ARTICLE IN PRESS

PERGAMON

Progress in Quantum Electronics ▮ (▮▮▮▮) ▮▮▮–▮▮▮

Progress in Quantum Electronics

www.elsevier.com/locate/pquantelec

Lasing in chiral photonic structures

Victor I. Kopp[a,*], Zhao-Qing Zhang[b], Azriel Z. Genack[a,c]

[a] *Chiral Photonics, Inc., Clifton, NJ 07012, USA*
[b] *Hong Kong University of Science and Technology, Clear Water Bay, Kowloon, Hong Kong*
[c] *Queens College of CUNY, Flushing, NY 11367, USA*

Abstract

This article presents a review of the lasing and photonic properties of periodic one-dimensional anisotropic structures with the symmetry of a double helix. Examples are self-organized cholesteric liquid crystals (CLCs) and sculptured thin films created by vapor deposition. A reflection band with sharp, closely spaced transmission peaks at its edges occurs for circularly polarized light with the same handedness as the helical structure. Within the reflection band, this wave is evanescent, corresponding to a vanishing density of states (DOS). Oppositely polarized light is uniformly transmitted. Since optical emission is proportional to the DOS, it is suppressed within the reflection band. However, it is enhanced at the band edge, where a series of narrow long-lived transmission modes are found. For this reason lasing in dye-doped CLCs occurs at the edge of the stop band rather than at its center, where reflection is highest. Introducing an additional rotation or an isotropic layer within a chiral structure creates a single circularly polarized localized mode with the same handedness as the structure. A resonance appears in the transmission of light of this polarization in thin samples. In thicker samples, the resonance appears instead in the reflection for oppositely polarized light. In contrast to strong modulation of the intensity within the sample on a wavelength scale, a characteristic of layered dielectric medium, the intensity within a chiral medium varies slowly when the sample is excited either at the band edge or at a localized mode. A transverse coherence is created in emission over a length scale proportional to the square root of the photon dwell time at resonance with long-lived modes. This makes possible spatially coherent lasing over a large area in thin films. The photonic properties of chiral thin films make them promising candidates for a variety of filter and laser applications.

*Corresponding author.

0079-6727/03/$ - see front matter © 2003 Published by Elsevier Science Ltd.
doi:10.1016/S0079-6727(03)00003-X

Contents

1. Photonics of periodic structures 000
1.1. Introduction 000
1.2. One-dimensional periodic structures 000

2. Cholesteric structures 000
2.1. Cholesteric liquid crystals 000
2.2. Sculptured thin films 000

3. Stop bands in cholesteric media 000
3.1. Wave propagation 000
3.2. Measurement of density of photonic states 000

4. Band-edge lasing 000
4.1. Band-edge modes 000
4.2. Spectral and temporal measurements of emission and lasing . 000
4.3. Discussion 000

5. Spatial coherence 000
5.1. Oblique incidence 000
5.2. Spatial measurements of laser emission 000
5.3. Theory and simulations 000
5.4. Diffusion of coherence 000

6. Chiral twist defect 000
6.1. Defects in periodic media 000
6.2. Modeling and simulations 000
6.3. Optical and microwave measurements 000
6.4. Discussion 000

7. Conclusion 000

Acknowledgements 000

References 000

1. Photonics of periodic structures

1.1. Introduction

Coherent scattering of the electronic wavefunction in the periodic potential of the crystal lattice produces a sufficiently large gap in the electronic energy spectrum of semiconductors such that the valence band is nearly filled while the conduction band is nearly empty (Fig. 1). Since few holes exist in the valence band, the rate of electron–hole recombination is low and electron states are long lived. Because the electron density in semiconductors can be externally controlled, these materials have become widely used platform for modern electronics and photonics. Control of the electron density is achieved by doping with n or p-type impurities that may, respectively, release electrons into the conduction band or trap electrons from the

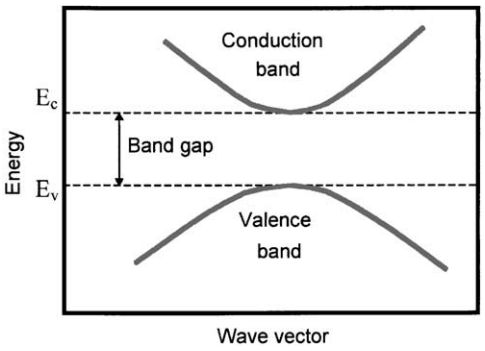

Fig. 1. Energy-wave vector diagram for semiconductor.

valence band to create holes. Electronic densities are also controlled by applying a voltage across a p–n junction. Light is emitted when electrons in the conduction band recombine with holes in the valence band. When the rate of electron and hole injection at a p–n junction and the lifetime of photons in the gain region are sufficiently high, lasing ensues. Optical feedback is a critical parameter in determining the laser threshold.

In analogy with the energy gap in semiconductors, a photonic bandgap (PBG) may appear in the spectrum of propagating electromagnetic modes in periodic structures [1–3]. Within the bandgap, the wave is evanescent and decays exponentially, so that the density of states (DOS) within the gap vanishes in large structures. Since the rate of spontaneous emission is proportional to the DOS, spontaneous emission is suppressed within the gap [1,2]. A schematic illustration of a periodic 3D dielectric structure is shown in Fig. 2a [3]. Modifying the sample so as to disrupt the periodicity of the structure can produce a long-lived and hence spectrally narrow defect mode within the gap, as shown in Fig. 2b.

Yablonovitch has predicted that low-threshold lasing will occur at defect modes within the bandgap of photonic crystals (PCs) since the excitation energy will not be drained by spontaneous emission into modes other than the lasing mode [2]. Lasing is further facilitated at the wavelength of the defect mode since the photon dwell time is enhanced, giving ample opportunity for amplification by stimulated emission. This has stimulated a considerable effort to produce PBG structures [4–7]. A wide variety of PCs possessing PBGs have been produced in one, two and three dimensions from microwave to optical frequencies [3–7]. These materials facilitate the control of optical propagation, spontaneous emission, and lasing and may therefore be expected to exhibit novel quantum optics behavior. There are also prospects for new optical devices exploiting both the electronic bandgap due to periodicity on the scale of the electronic wavelength and the PBG arising from the periodicity on the scale of the electromagnetic wavelength.

One-dimensional periodic structures always produce bandgaps, whereas 1D periodicity of dielectric layers embedded in three-dimensional space produces a stop

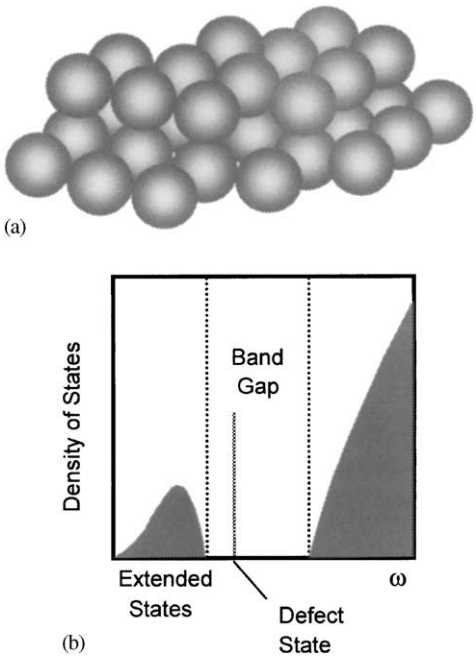

Fig. 2. (a) 3D photonic crystal and (b) DOS. A defect state is created when the periodic structure shown in (a) is disrupted.

band centered on the direction perpendicular to the layers. The existence of a complete bandgap is not guaranteed in two and three-dimensional periodic structures. The ratio of the width of a gap to the midgap frequency depends, in general, upon the lattice structure, dielectric contrast, topology (connectivity) in a unit cell, and the filling ratio of the dielectric component. Two-dimensional PCs with cylindrical inclusions have attracted considerable attention. Light may be confined vertically in these structures by using a semiconductor waveguide [3,6]. Such systems can be fabricated down to sub-micron length scales using conventional fabrication techniques and can therefore be used in optical components.

Creating a complete gap in three dimensions presents a considerable challenge. Collections of spherical colloidal microparticles spontaneously order on a face-centered cubic (fcc) lattice [8] and in nature this process leads to gemstone opals. However, these structures only form partial bandgaps. A complete bandgap at achievable dielectric contrast was predicted for the diamond structure [9]. Later, additional systems were shown to exhibit complete bandgap, such as the 'three-cylinder' structure proposed by Yablonovitch et al. [10] that may be produced by "drilling" and the layer-by-layer structure proposed by the Ames group [3–5]. In addition, a 3D photonic crystal can be produced in the blue mesophase of liquid crystals [11] leading to lasing in this material with an incomplete bandgap [12]. However, because such artificial dielectric microstructures are difficult to produce on the micron or sub-micron scale required in optical devices, a variety of approaches

have been considered. For example, inverted opal structures have been produced by filling the interstitial spaces between ordered spheres with high-dielectric materials and then etching or burning away the spheres [3–5]. When the dielectric contrast is large enough, one or more complete bandgaps will open [13,14].

In contrast to the difficulty of producing samples with a 3D PBG, one and two-dimensional bandgap materials are readily fabricated. In these structures, the excited state lifetime may often be only marginally modified since the rate of spontaneous emission is changed only around some direction or plane. Below the lasing threshold, population inversion may not therefore be significantly affected by the periodic structure. However, the dwell time within the sample for emitted photons is still substantially enhanced near the band edge in 1D periodic structures. This may substantially suppress the lasing threshold. Dowling et al. have predicted that low-threshold lasing should occur at the edge of a photonic stop band of a 1D periodic structure because the group velocity near the band edge is substantially reduced and the photon dwell time is correspondingly enhanced [15]. In thin samples, propagation is governed by the interaction with discrete modes rather than by a monotonic dispersion relation within a pass band. The dwell time is therefore a strongly modulated function of frequency. Tocci et al. found that the presence of a stop gap in a 1D structure results in an alteration of the spontaneous emission spectrum of a GaAs light emitting diode sandwiched between stacks of distributed Bragg reflectors [16]. Lasing at the band edge and a suppressed DOS of waves propagating in the direction of the periodic modulation were observed in dye-doped cholesteric liquid crystals (CLCs) [17].

Many applications of PCs have been considered. If a single defect is introduced into an otherwise perfect PC, a localized defect mode (or a group of defect modes) may appear at a frequency inside the bandgap. Such cavity modes formed from a single defect can be utilized to produce low-threshold lasing. The vertical cavity surface-emitting laser (VCSEL), in which an optical mode is sharply peaked near a defect layer between two sets of distributed Bragg reflectors occurring within a post, is a direct demonstration of this principle [18]. A laser cavity formed from a single defect in a two-dimensional PC has also been demonstrated [19].

If a line defect is introduced into a PC, an extended waveguide mode is created that can guide light [20]. A waveguide formed by a line defect in a PC functions via a different mechanism than waveguides such as optical fibers, which are based on total internal reflection. In traditional optical fibers, light escapes at bends if the turn is so sharp that the angle of incidence of light as it impinges upon the side of the fiber is smaller than the angle of total internal reflection. However, for a PC waveguide, the wave can be guided even around tight corners without spreading in the transverse direction since wave confinement is a result of Bragg reflection [20]. Nearly perfect transmission at sharp bends has been demonstrated experimentally in a two-dimensional PC made of alumina rods arranged in a square lattice in air background [21]. The use of PCs to achieve waveguide branches and waveguide crossing, resonators, and wavelength division multiplexing has also been studied intensively in recent years [22]. PCs are also being developed as narrow-band frequency filters, high-reflectivity mirrors, low-loss resonant cavities, directional antennas and PC

fibers, etc. [3–5]. PC fibers provide another way to guide light. In this case, a single defect is introduced into a two-dimensional PC and the light is guided through the defect in the third direction by Bragg reflection instead of total internal reflection in optical fibers [23]. Advances in these areas have facilitated the realization of all-optical circuits.

The discussions above have been devoted to PCs made of linear materials. Important applications could be developed by dynamically tuning the properties of PBGs via an excitation beam. For instance, Scalora et al. [24] studied the optical-limiting behavior of a Kerr-nonlinear quarter-wave reflector, using the beam-propagation method. The mechanism may be briefly described as follows. The width of the bandgap is proportional to the difference in the dielectric constants of the two media. By doping a sample to induce a Kerr nonlinearity so that the effective dielectric constant depends on the electromagnetic field intensity, $\varepsilon_{\text{eff}} = \varepsilon + \chi^{(3)}|E|^2$, the width of the gap can be altered dynamically. A probe beam operates near the band edge and a strong pump beam capable of altering the index of refraction of the nonlinear quarter-wave reflector operates in the transmission band. The pump beam is used to control the position of the band edge of the nonlinear quarter-wave reflector thereby modulating the transmission and reflection of the probe beam.

Excitation of nonlinear media with high power lasers may create localized states with frequencies in the forbidden gaps, known as gap solitons. This term was first introduced by Chen and Mills [25] in a numerical study of 1D superlattices with one film in each unit having a Kerr nonlinearity. The electric field envelope inside the medium resembles a hyperbolic secant function, reminiscent of solitary wave solutions of the nonlinear Schrödinger equation. Later, Mills and Trullinger [26] found an analytical solution for stationary gap solitary waves in the framework of the coupled-mode theory, which assumed that the refractive index is weakly modulated (the so-called shallow-grating case). Propagating gap solitary wave solutions have also been found analytically [27]. Both gap solitons and traditional optical fiber solitons emerge from the interplay between the group velocity dispersion (GVD) and the nonlinearity of the medium. However, GVD in fibers is mainly due to the frequency dependence of the effective refractive index, whereas in the latter, GVD is due to the periodic variation in the dielectric constant. The latter variation can be many orders of magnitude larger than the variation in the dispersion in optical fibers. Gap solitons also differ from fiber solitons in that they may attain any velocity between zero and the average speed of light of the uniform medium, whereas fiber solitons travel with the average speed of light in the medium.

Using the coupled-mode theory, which is valid in the case of small modulation of the dielectric function, John and Aközbek [28] obtained solitary waves in calculations for 2D and 3D Kerr-nonlinear PCs. Recently, Mingaleev and Kivshar [29] demonstrated the existence of stable gap solitons in 2D PCs with large dielectric contrast. They showed that it is possible to realize bistable and multistable behavior with gap solitons. Centeno and Felbacq [30] demonstrated numerically bistable behavior of a defect mode inside a finite-size 2D nonlinear photonic crystal.

Sum-frequency generation and second-harmonic generation can occur in PCs with $\chi^{(2)}$-nonlinearity. By making use of both the high electromagnetic mode density at

the band-edge and the nearly perfect phase-matching in PCs, Scalora et al. [31] found numerically that the second-harmonic-generation efficiency in a 1D periodic structure can be enhanced by several orders of magnitude over that produced by an equivalent length of a phase-matched bulk medium. This has important applications in high-energy lasers, Raman-type sources, and frequency up- and down-conversion schemes.

1.2. One-dimensional periodic structures

A particularly simple PC is a 1D system consisting of alternating layers of material with dielectric constants, ε_a and ε_b (refractive indices, $n_a = \sqrt{\varepsilon_a}$ and $n_b = \sqrt{\varepsilon_b}$), and layer thicknesses, a and b. Many analytical results have been obtained for the optical properties of such multilayer systems [32,33]. A special case of such a multilayer system is the quarter-wave stack, which is normally called a distributed Bragg reflector. In this case, the optical path in each layer is exactly $\frac{1}{4}$ of the midgap wavelength, λ_0. The midgap frequency, ω_0, is given by, $n_a a = n_b b = \lambda_0/4 = \pi c/2\omega_0$. It is useful to consider the optical properties of the quarter-wave stack. For simplicity, we assume the material is both dispersionless and lossless. Since a multilayer system is homogeneous in the transverse $x-y$ plane, all wavefunctions along this plane are plane waves and can be indexed by $k_\parallel$. There exist no bandgaps in the $x-y$ plane. In the layering direction, however, wavefunctions are Bloch waves and stop bands exist. Here we will focus on the case of light propagating normal to the plane, $k_\parallel = 0$. The time-independent Maxwell's equation then has a simple scalar form:

$$\frac{\omega^2 \varepsilon(z)}{c^2}\psi(z) + \frac{\mathrm{d}^2}{\mathrm{d}z^2}\psi(z) = 0, \tag{1}$$

where $\varepsilon(z)$ is a function with period $d = a + b$. The wavefunction ψ represents the electric or magnetic field and has the Bloch form $\psi(z) = \mathrm{e}^{\mathrm{i}Kz}u_k(z)$, where K is the Bloch wavevector and u_k is a periodic function of period d. The dispersion relation, $\omega(K)$, is determined by the equation [32]:

$$\cos(Kd) = \cos(k_a a)\cos(k_b b) - \frac{1}{2}\left[\frac{k_a^2 + k_b^2}{k_a k_b}\right]\sin(k_a a)\sin(k_b b), \tag{2}$$

where $k_a = n_a\omega/c$ and $k_b = n_b\omega/c$. Propagating modes are allowed if the right-hand side of Eq. (2) has an absolute value less than or equal to unity so that the value of K is real. The band-edge states occur when $Kd = m\pi$ for any integer m, so that $\cos Kd = \pm 1$. At the band edges, the wavefunctions are standing waves. Inside a bandgap, Eq. (2) yields a complex wavevector K corresponding to a decaying wave. The DOS diverges as the band edge is approached as an inverse square root and vanishes inside the bandgap. The standing waves at the lower and upper edges have the same value of K but are mutually orthogonal [32]. For example, at the lower edge of the first bandgap, where $Kd = \pm\pi$, the energy density (or $|\psi|^2$) is concentrated in layers with a higher value of the refractive index. For the upper band edge, on the other hand, the energy density (or $|\psi|^2$) is concentrated in layers with a lower value of

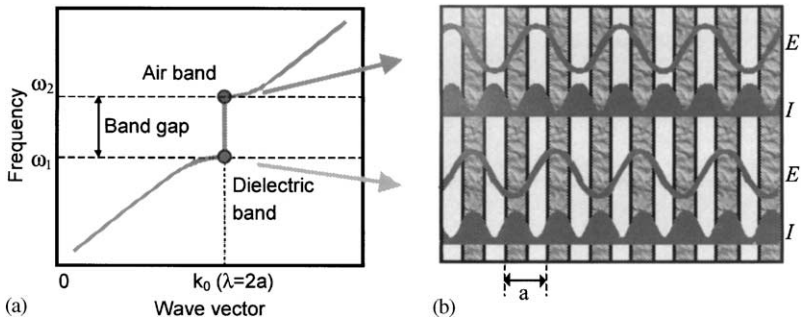

Fig. 3. (a) Photonic band structure of a layered dielectric system with period a. (b) Dark and light layers correspond to high and low refractive indices, respectively. The electric field (E) and intensity (I) near the center of the sample are shown.

refractive index as illustrated in Fig. 3. Thus, the first pass band is normally called the dielectric band, since the energy is concentrated in the higher dielectric material while the second band is called the air band [3]. The variation of energy density in the components of the structure with different dielectric constant is not limited to 1D PCs. It is a generic property of Maxwell's equation in 2D and 3D PCs as well. Other generic properties of PCs are scaling properties, which hold when the material is dispersionless [3]. In this case, if we compress or expand a PC by a scale parameter s, i.e., $r' \to sr$, Maxwell's equations are unchanged if the frequency is scaled as $\omega' \to \omega/s$. The same frequency scaling can be achieved if we multiply the dielectric constant by a factor, i.e., $\varepsilon(r) \to s^2\varepsilon(r)$. These scaling relations can easily be seen from Eq. (1).

The above discussions briefly summarize some intrinsic properties of the PBG behavior in an infinite multilayer system. In reality, a multilayer PC is always of finite thickness. The wave in the medium may be expressed in terms of quasi-modes of finite linewidth due to coupling to the boundaries. The transmission spectrum displays the resonant coupling via these modes. Below, we briefly discuss the transmission behavior near the band edge.

The transmission properties of an N-period multilayer system embedded in air can be obtained by using the transfer-matrix method [33]. For an incident plane wave, the transmitted field can be expressed as $t_N(\omega) = |t_N(\omega)|e^{i\phi_N(\omega)}$. If we write the accumulated phase as $\phi = kNd$, the phase velocity and group velocity can be defined as $v_p = \omega/k$ and $v_g = d\omega/dk$, respectively [34]. The density of modes can be defined as $\rho_N(\omega) = dk/d\omega$, which is the reciprocal of the group velocity. Analytical results for the transmission coefficient, $T_N(\omega) = |t_N(\omega)|^2$, and $\rho_N(\omega)$ have been obtained as a function of the Bloch phase of an infinite-period system, β, which depends upon the frequency via the relation $Re\{1/t(\omega)\} = \cos\beta$. Here $t(\omega)$ is the transmission amplitude of a unit cell [33]. Using these analytical results, some general properties can be obtained. Both $T_N(\omega) = |t_N(\omega)|^2$ and $\rho_N(\omega)$ exhibit a series of $N-1$ resonances in each pass band. The transmission is unity at the peak of each resonance. The maximum and minimum values of T_N and ρ_N coincide when N is large. The function $\rho_N(\omega)$ has its largest value at modes closest to the edges of the band, where the line is the narrowest and the dwell time is the greatest. This reflects

the accumulation of energy inside the sample. Thus, the band-edge resonance is favorable for lasing. The enhancement of emission at the band edges and the suppression of spontaneous emission within the stop band was observed from a GaAs light emitting diode sandwiched between stacks of distributed Bragg reflectors [16]. The DOS in a 1D PC was measured in dye-doped CLC, giving good agreement with a calculation of $\rho(\omega)$ [17]. Low-threshold band-edge lasing was also observed in this structure [17]. A comparison of optical properties of CLC with those of layered dielectric media shows that the CLC structure exhibits a wider bandgap and narrower linewidths for modes near the band edge than does the layered dielectric structure with the same index contrast and thickness [35]. These results suggest that CLCs are promising PBG materials for lasing, switching and display applications.

2. Cholesteric structures

In this section, we consider two helical structures with the symmetry property required to create a stop band that the pitch equals twice the period, $P = 2a$. CLCs may be synthesized by allowing an appropriate chemical mixture to self-organize. CLC structures also occur naturally in some species of beetles. Sculptured thin films (STFs) are fabricated in a continuous deposition process.

2.1. Cholesteric liquid crystals

The layered structure of the cholesteric phase of liquid crystals is similar to that of nematic liquid crystals. However, because it is composed of chiral molecules, which can be either left or right handed, the lowest energy configuration is achieved with a rotation by a small fixed angle between consecutive molecular layers [36–38]. Since the dielectric constant of a particular layer and of a layer rotated by 180° are the same, the structure has double helix symmetry. As a result, the pitch of the structure, which is the distance in which the director rotates by 360°, is twice the period of the cholesteric structure, as seen in Fig. 4. The energy of the twist is smaller of the energy

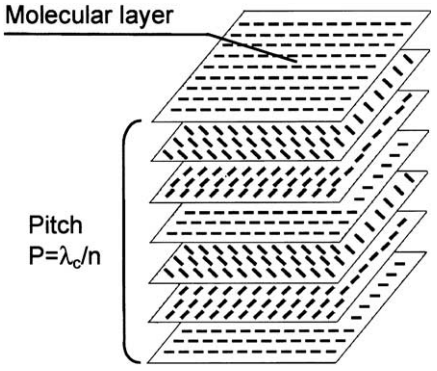

Fig. 4. Molecular structure of CLCs. The dashes indicate the orientation of the director.

associated with in-layer interaction by a factor of order 10^5 [39]. As a result, a helical structure is created once the liquid crystal is placed between two glass substrates along which the CLC layers have a preferential orientation. This is achieved by coating both substrates with a polymeric alignment layer and then buffing the surface.

Fig. 4 illustrates the molecular ordering of a CLC. The rod-shaped molecules are arranged approximately parallel to each other. The average direction of the long molecular axis in the plane is called the director. The refractive indices for light polarized parallel and perpendicular to the director are the extraordinary and ordinary indices, n_e and n_o, respectively. For sufficiently thick films, the reflectance of normally incident, circularly polarized light with the same sign of rotation as the CLC structure is nearly complete within a band centered at a wavelength within the medium equal to the pitch of the structure. This corresponds to a vacuum wavelength $\lambda_c = n\lambda_0 = nP$ where $n = (n_e + n_o)/2$. The reflected light has the same sign of circular polarization as the incident beam. This is in contrast to light undergoing Fresnel reflection from an isotropic medium for which the sense of circular polarization is reversed. Modeling the sample as a series of thin rotated anisotropic layers, de Vries showed that the width of the reflection band is given by, $\Delta\lambda = \lambda_c \Delta n/n$, where $\Delta n = n_e - n_o$ [38]. The band structure of a CLC at oblique incident angle was calculated in Ref. [40]. A typical reflection spectrum from CLC film for polarized light with the same sense of circular polarization as the sample structure is shown in Fig. 5 [41]. This behavior differs from that in binary layered (BL) structures in two respects: first, the bandgap exists only for a single circular polarization and second, there is only a single gap. In systems with a periodically varying pitch, however, Bermel and Warner have shown that additional bandgaps appear for light of both circular polarizations [42].

2.2. Sculptured thin films

Unlike CLCs, which are self-organized structures, STFs can be fabricated. A multicolumn thin film develops on a rotating substrate, which is oriented at an

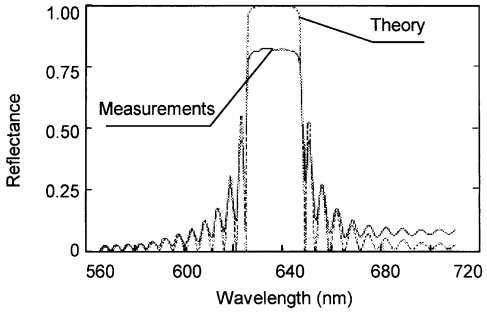

Fig. 5. Measured reflection spectrum from a monodomain CLC superimposed upon calculated spectrum (adapted from Ref. [41]).

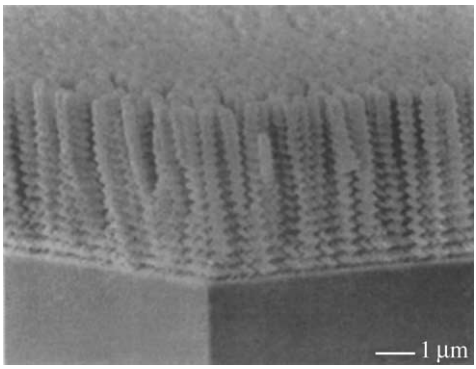

Fig. 6. SEM photograph of a sculptured thin film [43].

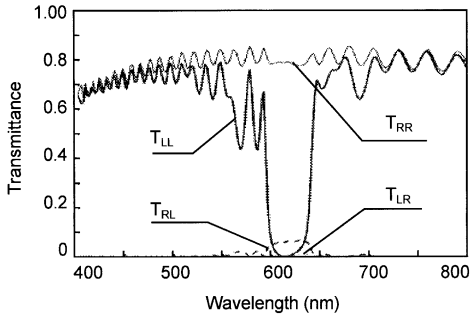

Fig. 7. Measurement of polarized transmittances of a left-handed STF [45].

oblique angle to a vapor stream. An example of an STF is shown in Fig. 6 [43]. While this structure possesses helical rather than double helical symmetry, it has optical properties similar to those of CLCs [44] for light propagating along the helical axis. Measurements by Wu et al. [45] of transmission through a left-handed STF grown of titanium oxide on a glass substrate are shown in Fig. 7. The thin film is 5.2 μm thick and is deposited as the substrate turns 15 times. Its average refractive index is 1.77. The right circularly polarized (RCP) component of transmittance for left circularly polarized (LCP) incident light is denoted T_{RL} and other terms are similarly indicated. Simulations for an index-matched STF give $T_{RL} = T_{LR} = 0$ and $T_{RR} = 1$.

3. Stop bands in cholesteric media

3.1. Wave propagation

It is useful to compare the results of computer simulations of light propagation in a CLC and in a layered dielectric medium. The CLC is modeled as a set of anisotropic layers of equal thickness, which are significantly thinner than the

wavelength of light. The directions of the axes of optical indicatrix are rotated by the same small angle within the plane of the layer between successive layers. Using the scattering matrix approach, we calculate the transmission and reflection from a single layer as well as the transmission and reflection from $n+1$ layers in terms of n layers. By induction, it is then possible to simulate wave propagation through a CLC sample of any thickness. Layered dielectric structures can also be simulated using this approach by replacing anisotropic with isotropic layers. These simulations give the transmittance and reflectance spectra of the CLC and of the layered dielectric structure as well as the distribution of the optical intensity inside these media. It is also possible to calculate the spatial distribution for a given direction of propagation and sense of circular polarization. The electric field along a plane within the sample can be obtained by dividing the structure into two parts bounded by this plane. Using the calculated reflectance and transmittance for each of the parts, as well as for the entire structure, we find the field in the selected plane. Propagation of circularly polarized light with a sense of rotation opposite to the rotation of the CLC structure is only slightly affected by the chiral structure, whereas circularly polarized light with the same sign as the CLC rotation is nearly totally reflected within a certain frequency range. Within this reflection band, the intensity falls exponentially and the light is a pure standing wave without a traveling wave component. This corresponds to a pure imaginary wave, which does not contribute to the DOS.

It is of interest to compare the properties of waves in CLCs and in layered dielectric media. Wavelength scale oscillations of the electromagnetic energy found in layered dielectric media (Fig. 3) are greatly suppressed in CLCs. Although the energy density is not rapidly modulated, the direction of the electric field of the standing circularly polarized wave, with the same sign of rotation as the CLC structure itself, rotates in space with pitch P since the electric field is always parallel (perpendicular) to the molecular director at the low (high) frequency edge of the stop band. As a result, the field experiences only an index of n_e (n_o) (Fig. 8). Of course, the electric field, for this standing circularly polarized wave, oscillates in time, but, unlike a traveling circularly polarized wave, the direction of the field does not oscillate.

Fig. 9 shows transmittance spectra calculated for layered and CLC structures with refractive indices of 1.47 and 1.63, period $a = 0.2\,\mu m$ and a total thickness of $16\,\mu m$. In the layered dielectric material, the indices correspond to those of the two equal thickness layers, whereas, in the CLC, these correspond to the ordinary and extraordinary indices. The results of the computer simulation of electromagnetic energy density for the first and second mode near the band edge are shown in Figs. 10 and 11, respectively. In general, the intensity has a number of local maxima equal to the mode number inside the medium. The slowly varying envelope corresponds to a standing wave associated with counter propagating Bloch waves. The absence of modulation for the intensity within the cholesteric sample, together with the slightly higher value of the peak intensity as compared with the layered sample yield a higher integrated intensity within sample. This corresponds to an increase in the DOS and the photon dwell time within the sample and consequently to a narrower linewidth, seen in Fig. 9.

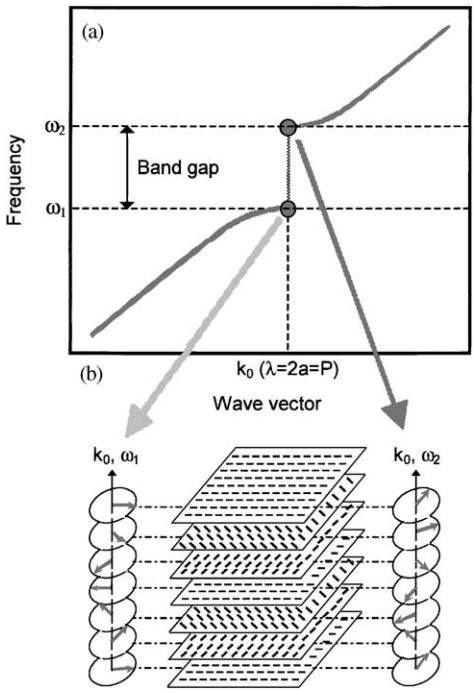

Fig. 8. (a) Photonic band structure of a CLC with period a and pitch $P = 2a$. (b) Arrows indicate the electric field direction being aligned along or perpendicular to the director.

The stop band shifts with oblique angle to higher frequency. As a result, the mode closest to the high-frequency band edge becomes isolated in angle as well as frequency. Using the transfer matrix approach, described in Section 5.3 below, transmission through the CLC film can be calculated versus both oblique angle and wavelength (Fig. 12). Transmission spectra at normal incidence, such as seen in Fig. 9, correspond to the results along the vertical line in Fig. 12. In Section 5, we show the way in which the angular dependence is reflected in the transverse spatial distribution of light transmitted through or emitted from a 1D periodic structure. This can lead to a wide coherence area in lasing from a thin film.

3.2. *Measurement of density of photonic states*

Measurements of emission and lasing were carried out using the experimental setup shown in Fig. 13. The excitation source was the second harmonic of a Q-switched Nd:YAG laser with and without mode-locking. Individual mode-locked pulses were approximately 70 ps long. Single Q-switched pulses were 150 ns long with maximum pulse energy of $\sim$1 mJ. The energy of the pump laser pulse impinging upon the sample was controlled with use of an electro-optic attenuator. The pump beam was approximately 5 mm in diameter at the focusing lens. This gave spot diameters of approximately 40 and 20 μm for the 30 and 14 cm focal length lenses,

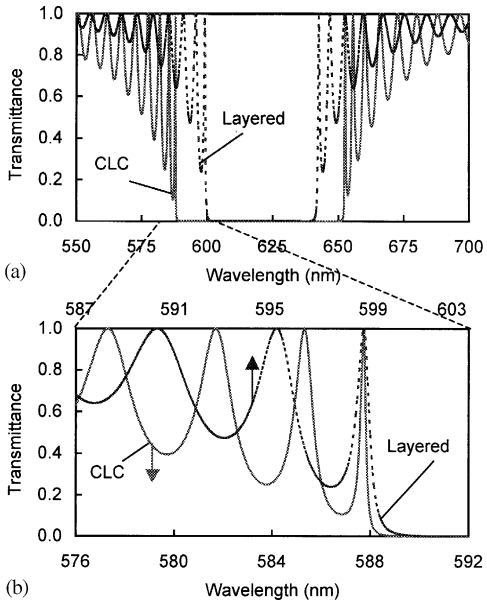

Fig. 9. Comparison of transmittance for BL and CLC structures in a large spectral range (a) and at the band edge (b). The spectra are shifted in (b) so that the peaks of the first mode at the band edge coincide.

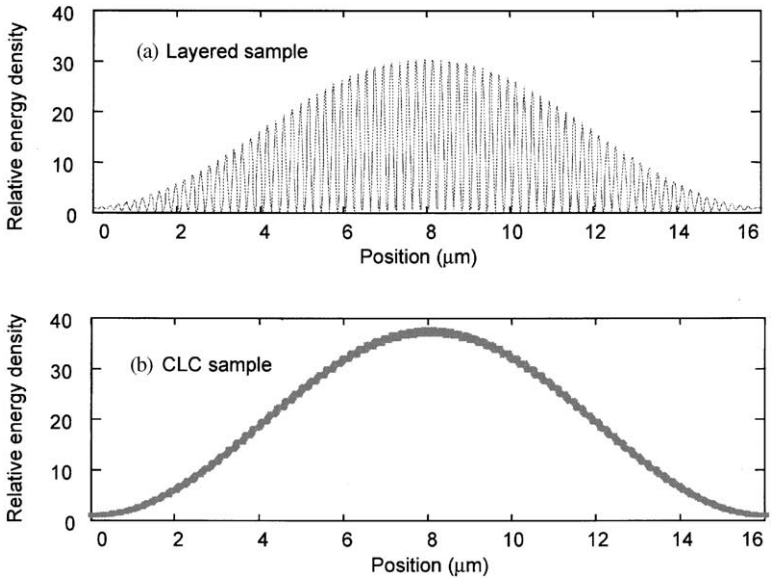

Fig. 10. Distribution of the energy density of the electromagnetic field inside a 1D periodic sample at the wavelength of the $n = 1$ mode for layered (a) and CLC samples (b). The refractive indices are 1.47 and 1.63 for the layers of the layered dielectric structure and for the ordinary and extraordinary indices of the CLC. The sample thickness is 16 μm and the period is 0.2 μm. The energy density of the incident wave is unity.

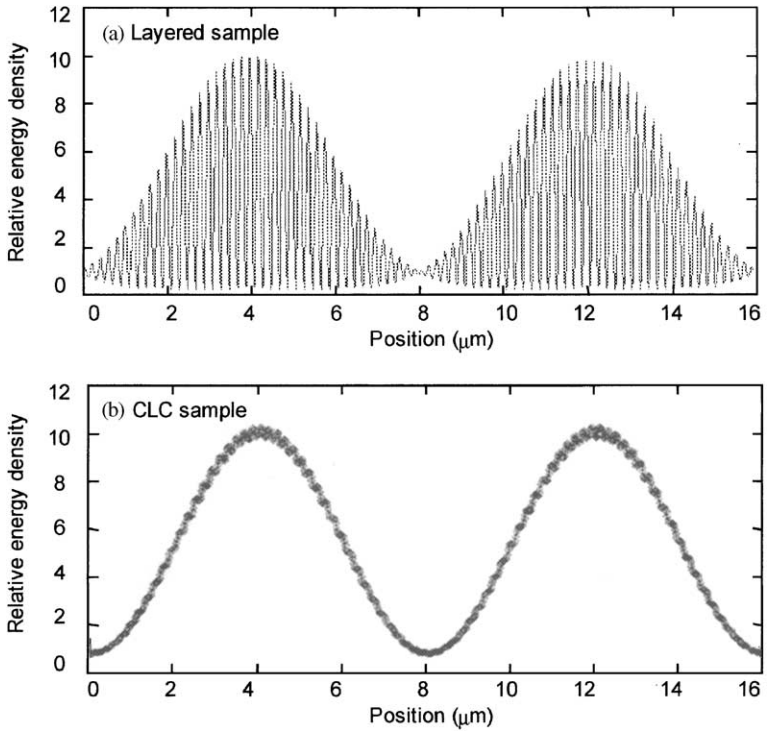

Fig. 11. Distribution of the energy density of the electromagnetic field inside a 1D periodic sample at the wavelength of the $n = 2$ mode for layered (a) and CLC samples (b). The parameters of the samples are the same as in Fig. 10.

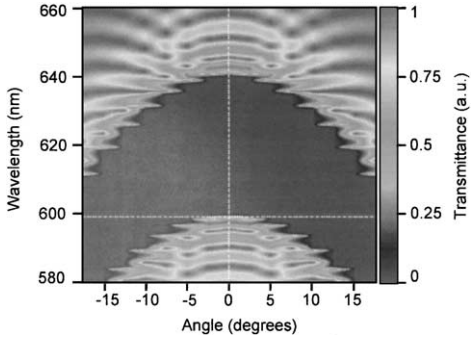

Fig. 12. Transmittance through CLC film versus frequency and oblique angels.

respectively. A lens with a focal length of 5.5 cm was used to collect the emitted light and to focus it onto the entrance slit of the spectrometer. This corresponds to collection angles of $\sim 30^\circ$ in air and $\sim 18^\circ$ within the CLC film. The emission was dispersed in a spectrometer and recorded using a CCD detector that captured a 74 nm band with a resolution of 0.075 nm.

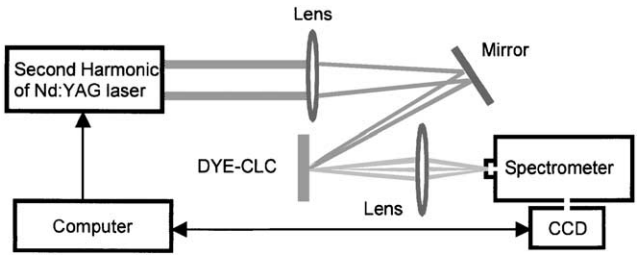

Fig. 13. Experimental setup for measurement of emission spectra of CLC films.

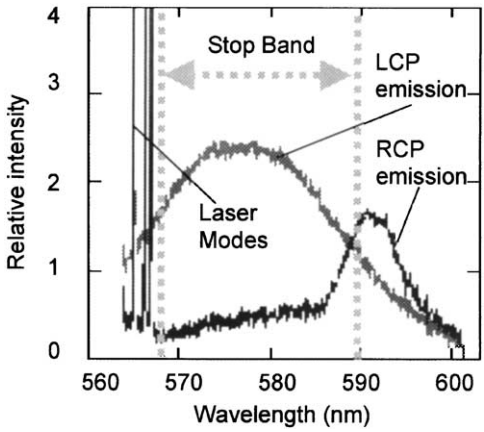

Fig. 14. Emission spectra from right-handed sample for LCP and RCP emission. The relative intensity of the lasing lines are ~50 units.

Measurements of LCP and RCP emission are shown in Figs. 14 and 15 for right and left-handed dye-doped CLC film, respectively. Since the matrix elements for spontaneous emission of LCP and RCP light are the same, and the light with handedness opposite to that of the structure is unaffected by the structure, a comparison of emission spectra of oppositely polarized radiation gives the ratio of the density of photon states. The rate of spontaneous emission of RCP light is inhibited within the band and enhanced at its edges in the right-handed sample as seen in Fig. 14 [17]. The same is true for spontaneous emission of LCP light in the left-handed sample (Fig. 15). The observed suppression of the DOS within the band and the sharp rise at the band edge are consistent with the calculated DOS in 1D structures.

The ratio of LCP to RCP spontaneous emission, shown in Fig. 15, gives the ratio of the density of photon states for these two polarizations for light emitted within the collection angle of the lens (Fig. 16). Since the DOS of RCP light is nearly uniform over this frequency range, being equal to $2Ln/c$ for light propagating perpendicular to the film, this ratio is proportional to the DOS of LCP light. These results are compared to calculation of the DOS in an unbounded structure. The DOS in a 1D

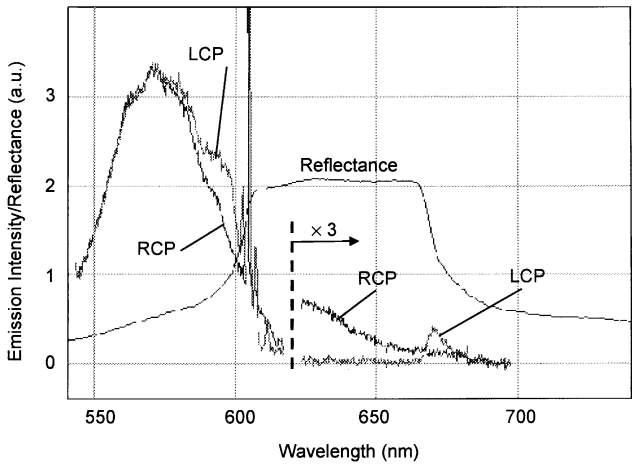

Fig. 15. Emission spectra from left-handed sample for LCP and RCP emission with superimposed reflectance spectrum.

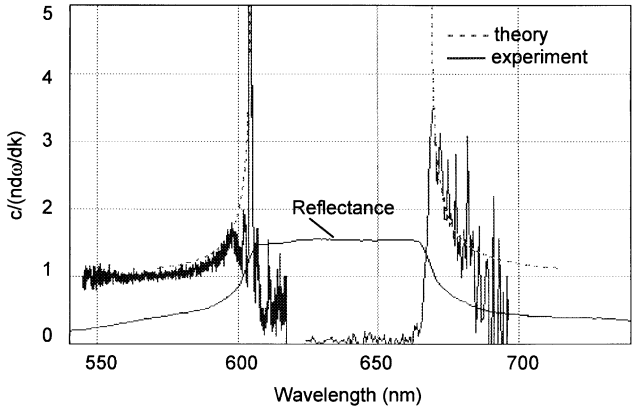

Fig. 16. Ratio of LCP to RCP emission spectra from left-handed sample and theoretical expression for DOS in an unbounded sample, $(c/n)/(\mathrm{d}\omega/\mathrm{d}k)$ in spectral region encompassing the stop band.

structure is proportional to $(c/n)/(\mathrm{d}\omega/\mathrm{d}k)$. In contrast to 2D and 3D structures, the DOS diverges at the band edge of unbounded 1D structures. This is seen in the calculated DOS shown in Fig. 16, which is given by the relations

$$n\omega(k)/c = \mathrm{sign}(k - k_0)\sqrt{k^2 - 2kk_0 + \omega_0^2} + \omega_0, \tag{3}$$

$$\omega_0 = 2\pi nc/\lambda_c, \quad \Delta\omega = \omega_0 \Delta n/n, \tag{4}$$

$$k_0 c/n = \sqrt{\omega_0^2 - (\Delta\omega/2)^2}. \tag{5}$$

Reasonable agreement is found between measurements in the CLC sample and the calculation of the DOS in an unbounded CLC. Sharp modes are not observed in spontaneous emission at the band edge because of the shift of emission spectra with angle.

Since one circularly polarized component of emission is suppressed within the stop band, whereas the other is allowed, doped CLCs films can serve as a source of circularly polarized radiation. Polarized spontaneous emission from luminophores at frequencies within the stop band was reported in polymeric CLCs [46]. This may find use as a polarized backlight in display applications [46].

4. Band-edge lasing

4.1. Band-edge modes

Because the gap only exists within a limited angular range, we expect that the lifetime of the molecular excited state may not be appreciably modified by the periodic structure. However, the photon dwell time for band-edge states that participate in lasing is dramatically lengthened. The lifetime decreases rapidly for modes shifted further from the band edge, as shown in Fig. 17c. We find that the

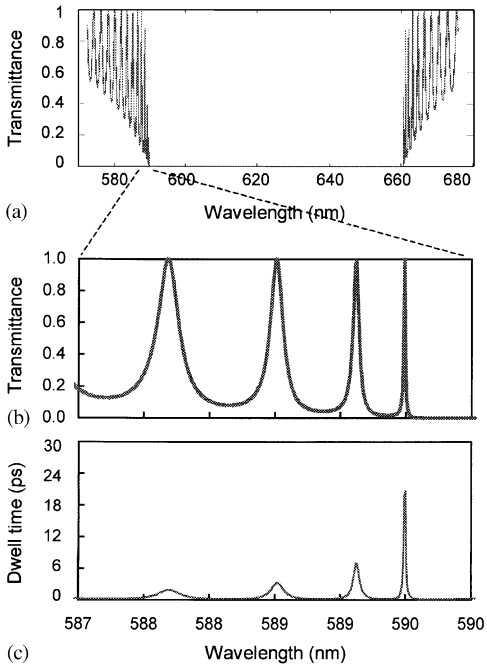

Fig. 17. Computer simulation of transmittance (a, b) and photon dwell time (c) through a 40-μm thick CLC film in a broad (a) and narrow (b, c) spectral range. Transit time through a homogeneous medium with the same thickness and average refractive index is about 0.2 ps.

threshold for lasing in particular modes increases with separation from the band edge. At the lowest powers, lasing occurs only for the mode closest to the band edge. The planar geometry of the 1D structure conveniently leads to diffraction limited lasing within a narrow cone normal to the CLC planes.

The use of dye-doped CLCs as thin film lasers was proposed nearly 30 years ago by Goldberg and Schnur [47]. It was first observed by Il'chishin et al. [48] and explained using distributed feedback theory [49]. Application of the theory would suggest that lasing would occur at the center of the reflection band near the Bragg frequency, as is the case in weakly modulated dielectric systems. The observation of lasing in CLCs far from the center of the reflection band was ascribed to distortions of the helical structure [50]. The explanation of the occurrence of lasing far from the center of the reflection band is that the reflection band is a true photonic stop band in which the DOS vanishes. Since emission is proportional to the DOS, it must vanish within the stop band. Emission and lasing would be expected to occur, however, in the series of narrow band-edge modes. These long-lived modes are shifted from the center of the reflection band.

At the wavelength of the first allowed mode in a 1D periodic structure, the transmittance is unity while the reflectance vanishes. Because of multiple internal reflections near the band edge, however, the photon dwell time for incident waves at the frequencies of modes at the band edge is significantly increased over the transit time through a homogeneous medium with the same thickness and average refractive index (Fig. 17c). At these modes, the wave is the sum of a standing wave inside the medium plus the incident wave. The lasing threshold is consequently lowered at these modes and is lowest for the first mode.

Figs. 17a and b show the results of a simulation of transmission through a 40 μm CLC sample. Distinct, closely spaced narrow modes are seen at the band edge. Fig. 18 shows the transmittance through a structure with the same variation of the real part of the dielectric function but with spectrally and spatially uniform negative imaginary component of the dielectric function corresponding to the critical gain for the first mode for which transmission diverges. Transmission for all other modes is only slightly greater than unity.

4.2. *Spectral and temporal measurements of emission and lasing*

Key properties of laser emission from dye-doped CLC films are shown in Figs. 19 and 20. A sharp laser line is seen at the edge of the reflection band. The reflection of approximately 50% of incident unpolarized light, seen in the reflection band, corresponds to nearly total reflection of the RCP component. The transmission shown is affected by both the selective reflection band and by absorption by dye molecules. The dye absorption is seen as the narrow dip of nearly 30% in transmission at a wavelength near 530 nm, close to the wavelength of the pump source. The laser line is clearly displaced from the frequency of peak reflection. A clear laser threshold in the input–output power dependence is seen in Fig. 20, unambiguously demonstrating the nonlinearity of band-edge emission. When the CLC structure itself can be optically pumped strongly enough that a population

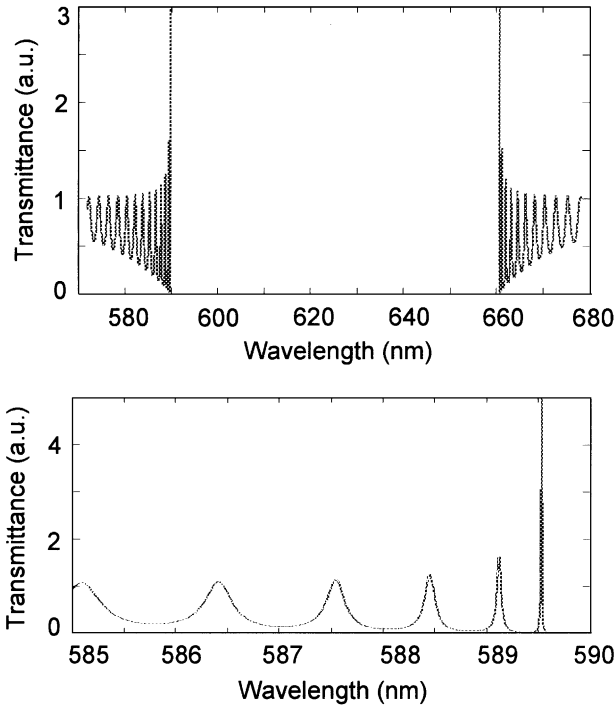

Fig. 18. Transmittance through the CLC film of Fig. 17 with gain in a broad (a) and narrow (b) spectral range.

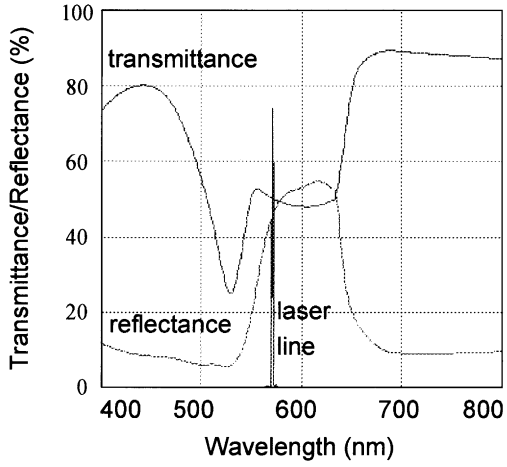

Fig. 19. Band-edge laser emission from dye-doped CLC film superimposed over low-resolution unpolarized transmission and reflection spectra.

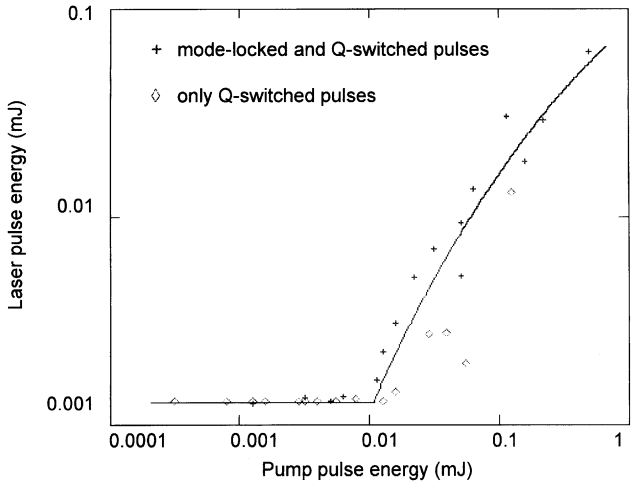

Fig. 20. The dependence of emitted laser power versus pump power for Q-switched and mode-locked pump pulses.

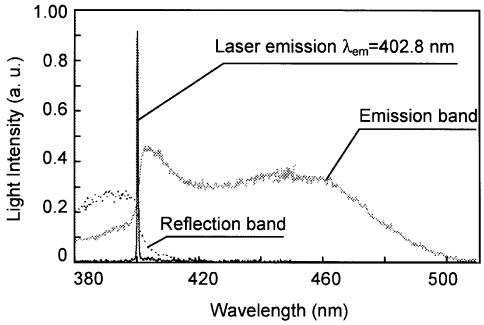

Fig. 21. Reflection band for unpolarized light, fluorescent emission spectrum below threshold (5-mm pump-beam diameter), and laser line (300-μm pump-beam diameter) for the BLO61-CB15 mixture. A different intensity scale was used for each of the three curves; they are shown in the same graph for the purpose of comparison [51].

inversion occurs, lasing may occur in an undoped sample. Muñoz, Palffy-Muhoray and Taheri demonstrated lasing from a CLC film without the addition of dyes under picosecond ultraviolet excitation [51]. A sharp laser line at the long-wavelength edge of the reflection band is observed as seen in Fig. 21.

We carried out measurements of lasing from two dye-doped CLC films doped with laser dye PM-597 (1,3,5,7,8-pentamethyl-2,6,-di-t-butylpyrromethene-difluoreborate complex) with different host compositions. The films possessed an absorption peak at 530 nm and an emission peak near 570 nm. Samples 1 and 2 have right- and left-handed helical structure, with thicknesses L of approximately 20 and 30 μm, respectively. The transmittance and reflectance spectra for normally incident

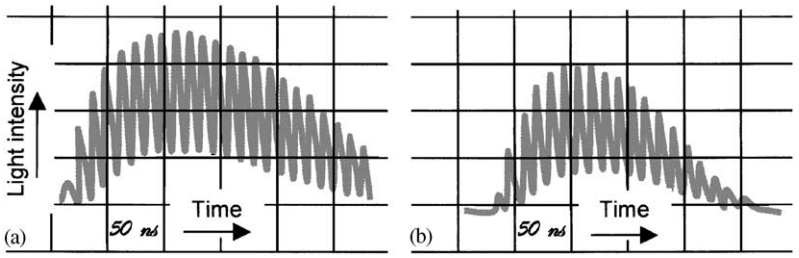

Fig. 22. Temporal structure of (a) pump and (b) laser emission from a CLC film.

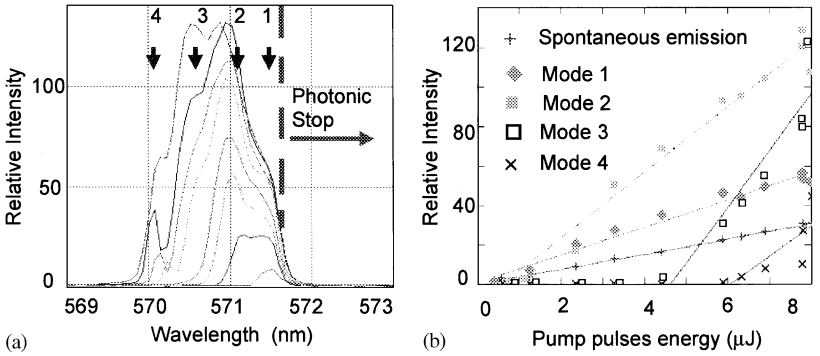

Fig. 23. (a) Mode structure of emission spectrum from sample 1 at different pump powers. (b) Relative intensities of emission for wavelength at frequencies indicated by the arrows in (a) correspond to peak intensity for four modes. The relative intensity scale is the same in (a) and (b).

unpolarized light for sample 1 are shown in Fig. 14. The band center is shifted to the red in sample 2 by approximately 40 nm relative to sample 1, as seen in Fig. 15.

The temporal structure of the emission was recorded with use of a photomultiplier tube placed at the position of the entrance slit of the spectrometer position in Fig. 13. The temporal resolution was 2 ns. Measurement of the temporal structure of the lasing and pump beams are presented in Fig. 22. The temporal envelope of the lasing train is narrower than that of the pump pulse because of the nonlinearity of the lasing process.

Spontaneous emission from a right-handed CLC sample for RCP and LCP light is shown in Fig. 14. RCP spontaneous emission is suppressed within and enhanced at the edges of the stop band relative to LCP emission. A set of narrow spectral lines with height of ~ 50 in arbitrary units on the scale of Fig. 14 is found at the high frequency band edge above a threshold in pump power. The divergence of the beam emitted from the sample is measured to be ~ 0.11 rad for a 20-μm diameter pumped spot. The radiation with the same sense of rotation as the CLC structure is emitted within the beam, while approximately 4% of the beam intensity is LCP. This corresponds to the expected change in helicity of RCP light upon Fresnel reflection from the glass–air interface. High-resolution spectra of band-edge emission at different pump power are presented in Fig. 23.

RCP laser emission spectra from sample 1 at various pump powers are shown in Fig. 23a for Q-switched pump pulses. At low pump power, a single laser line with a width of approximately 0.2 nm is observed near the stop band edge at 571.5 nm. Even at high pump powers, only a small number of closely spaced modes within a total width of $\sim$1 nm are involved in lasing. The laser linewidths appear to be inhomogeneously broadened in these samples pointing to a variation in pitch within the sample. The apparent central frequencies of the modes are indicated in Fig. 23a. The center of the laser emission at higher powers generally shifts further from the first mode at the band edge. The energy conversion efficiency from the pump to the laser beam is as high as 25% at a pump pulse energy of $\sim$0.1 mJ.

The spacing between modes shown in Fig. 23a is considerably less than the mode spacing of $\delta\lambda \approx \lambda_c^2/2Ln_{av} = 5$ nm in a homogeneous 20 μm thick film, reflecting the high DOS at the edge of the stop band [52,40]. The mode spacing does not correspond to those calculated for a periodic CLC. This may reflect the presence of disorder in the structure, which tends to shift and localize band-edge modes [53]. Since the modes are not strongly shifted into the stop band, the fluctuations in pitch may be assumed to be small. In the presence of strong disorder, lasing may arise due to modes that have been shifted far into the stop band.

The dependences of the output energy on pump power for the first four modes near the band edge of sample 1 are shown in Fig. 23b. For comparison, the linear dependence of the spontaneous emission integrated over the spectrum from 547 to 622 nm is also shown. Mode 1 at 571.5 nm, which is closest to the band edge, has the lowest lasing threshold. Lasing is observed at the lowest pump energies at which reliable spectral measurements are possible of 0.3 μJ. The thresholds for mode numbers 2, 3 and 4 peaked near 571.1, 570.5 and 570.2 nm, respectively, are seen to increase with increasing frequency shift from the band edge. The rate of increase of output power is seen in Fig. 23b to increase with mode number up to mode 3.

In sample 2, in which the reflection band is shifted significantly above the emission peak, lasing is observed only when the pump laser is both mode-locked and Q-switched. Polarized emission spectra from this sample are shown in Fig. 15. For reference purposes, the unpolarized reflectance spectrum at low resolution is also presented. LCP lasing again occurs at the blue edge of the reflection band, which is the edge closest to the emission peak. The peak intensity of the laser lines is 100 times greater than the maximum of the spontaneous emission. The RCP emission spectrum has a single broad peak and is similar to the emission spectrum expected for molecules within an unoriented host. On the other hand, LCP emission is suppressed in the reflection band and enhanced above the level of RCP emission at both edges of the band.

4.3. Discussion

A comparison of lasing, reflectance and transmittance spectra in Fig. 14 shows that lasing occurs at the edge of the photonic stop band. We find that shifting the edge of the stop band shifts the lasing frequency from approximately 560 to 610 nm in different hosts doped with the same dye. The divergence of the laser beam emitted

from sample 1 for pumped spot diameters of 40 and 20 μm is found to be ~0.06 and ~0.11 rad, respectively. This corresponds to a diffraction limited divergence for a coherent beam generated by spots with diameters of ~12 μm and ~7 μm, respectively. This appears to be consistent with a single coherent laser source, which is smaller than the pump diameter as a result of the nonlinear nature of lasing action. The laser radiation is RCP from sample 1 and LCP from sample 2 in conformity with the chirality of the CLC structure. Approximately 4% of the laser intensity is of opposite sign polarization. This is expected as a result of the change in chirality of light upon Fresnel reflection from the rear glass plate.

The distinction between the laser emission frequency, which occurs at the band edge and the peak of the spontaneous emission spectrum, allows for flexibility in the selection of the lasing frequency for any given dye. The lowest threshold would be produced when the dye emission peak is matched to the edge of the stop band. The dependence of the lasing frequency upon the position of the edge of the reflection gap suggests that the frequency of the laser can be modulated by an applied electric, magnetic or optical field or by temperature or pressure changes that modulate the CLC pitch, and hence, the frequency of the first band-edge mode.

Finkelmann et al. [54] observed lasing in dye-doped elastomeric CLCs, in which the reflection band shifts as the film is stretched. The lasing frequency could thus be tuned by stretching the film. However, the threshold found was orders of magnitude higher than in thermotropic CLCs. Apparently the disorder is so great in these films that the planar texture, which provides resonant feedback, is disrupted. Lasing is also observed in stiff chain polymeric lyotroic CLCs. Shibaev et al. [55] found that the lasing threshold in these materials is comparable to that in conventional thermotropic CLCs. The presence of longitudinal disorder as opposed to the specifically engineered distortion of the periodicity discussed in Section 6.1 may lead to the localization of light. Since the exponentially localized states have extended lifetimes within the medium, the laser threshold may be suppressed.

A comparison of the elements of a standard dye laser and of a dye-doped CLC laser is presented in Fig. 24. The compact nature of CLC structures, the ease with which they can be fabricated, as well as the absence of a need to align these systems suggest that they may be useful for producing microlasers and photonic devices.

5. Spatial coherence

5.1. Oblique incidence

A ring structure is observed in the far field of laser radiation at the band edge in CLCs. To understand its origin, we performed a study of the angular dependence of transmission in CLC films [56]. For normally incident plane waves, the first state on the high frequency side of the bandgap has the smallest line width. This facilitates single-mode lasing in this mode. For off-normal incident radiation, the gap position is found to shift to higher frequency. This places oblique waves at the frequency of the lasing mode at the high frequency band edge inside the stop band as seen in

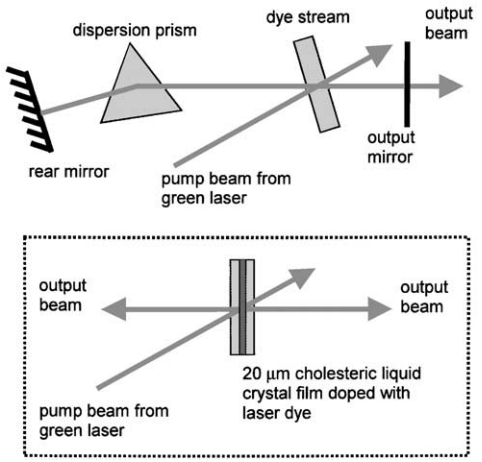

Fig. 24. Comparison of common dye-jet laser configuration and dye-laser based on CLC.

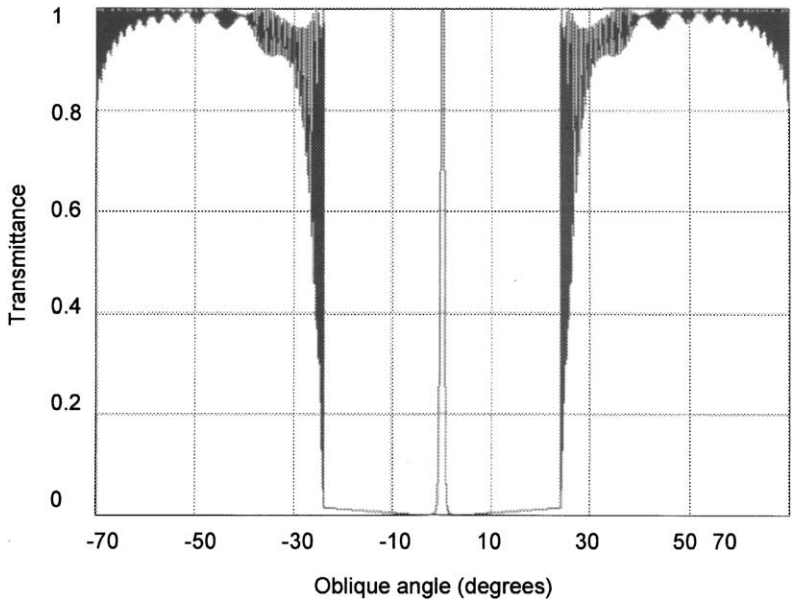

Fig. 25. Transmittance versus angle at the frequency of the first mode at the high frequency band edge.

Figs. 12 and 25. The transmitted radiation field is consequently confined to a narrow range of angles and radiation incident at larger angles is reflected. The restriction of the angular distribution of the transmitted wave for an incident Gaussian beam corresponds to a wide beam width at the output surface of the sample, which is inversely proportional to the divergence of the transmitted wave. This intensity

distribution has an exponential fall-off at the output surface of the sample, which results in a ring pattern in the far field, similar to the Fraunhofer diffraction of a plane wave by an aperture. In addition, we find a universal relation between the beam width at the output surface and the line width of the transmitted mode, which is valid not only for CLC films, but also for other layered media, such as BL systems.

5.2. Spatial measurements of laser emission

Measurements of the spatial distribution of the intensity emitted from a CLC sample were carried out using the experimental setup shown in Fig. 26. The CLC film studied was a right-handed structure with a thickness of 35 μm, $n \sim 1.7$ and $\Delta n \sim 0.2$. The samples were doped with laser dye PM-597 with an absorption peak at 530 nm and an emission peak near 600 nm. We pumped the sample with the second harmonic of Q-switched pulses of a Nd:YAG laser. The 150 ns pulses produced yellow radiation normal to the CLC sample planes. The emitted beam produced a ring pattern on a paper screen 11.5 cm from the sample, shown in Fig. 27. This pattern, whose appearance is similar to the optical Freedericksz effect, can be easily observed by eye. The optical Freedericksz effect can be observed when a laser beam passes normally through the film of a nematic liquid crystal [57]. But unlike that phenomenon which develops in time and involves the reorientation of the molecular directors, rings appear on a picosecond time scale.

5.3. Theory and simulations

The similarity of the experimentally observed ring structure to Fraunhofer diffraction from an aperture suggests that laser radiation emitted from a CLC film falls rapidly along the output surface and is directed in a narrow angular range about the normal direction. A theoretical analysis of the transmission was carried out to

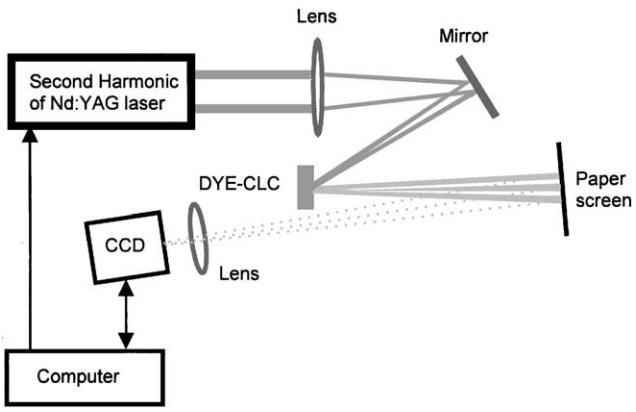

Fig. 26. Experimental setup for measurement of spatial distribution of the emission of CLC films.

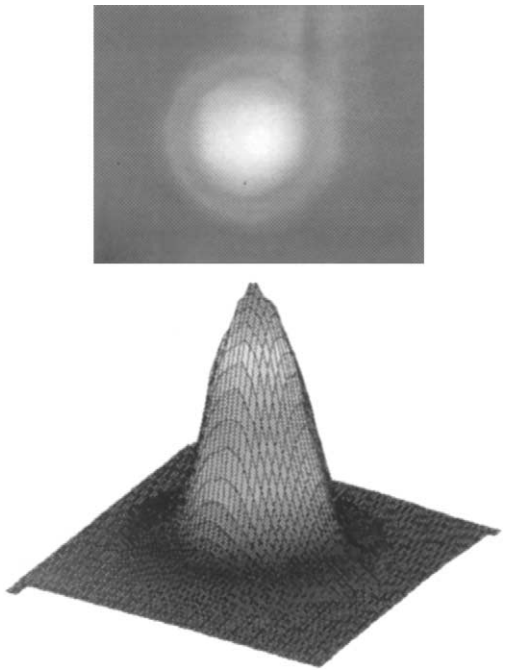

Fig. 27. Measurement of the spatial distribution of laser emission.

understand the origin of the angular confinement, as well as the ring structure and surface intensity distribution.

The sample is modeled as a set of thin, equal-thickness anisotropic layers. The director lies within the planes and rotates by a small angle between successive layers. A normally incident circularly polarized 1D Gaussian beam with the same handedness of circular polarization as the CLC film is incident upon the sample. The beam is constructed by superimposing plane waves at the same frequency as the lasing mode but with a Gaussian distribution of the amplitude with angle of incidence. The superposition of these plane waves leads to a Gaussian wave in 1D in the plane of incidence (the $x-z$ plane) with wave vector centered about the z-axis. The wave is homogeneous in the y-direction. The properties of the transmitted waves are calculated by using a 4×4-matrix method first introduced by Teitler and Henvis for anisotropic stratified media [58]. The method was later developed and applied to CLC and other liquid crystals by Berreman [59] and also by Wohler et al. [60]. The properties of the transmitted wave for each incident plane wave at a given incident angle are calculated. The superposition of all transmitted plane waves weighted by the Gaussian distribution of the incident beam gives the transmitted wave. The gain inside the CLC film is assumed to be uniform.

Let us consider a CLC sample with surfaces located at $z = 0$ and $z = L$. The sample is embedded in an isotropic background medium of refractive index n_b. A

continuous wave with frequency ω is incident upon the $z = 0$ plane at angle θ to the z-axis. Without loss of generality, we define the $x-z$ plane as the plane of incidence and write the dielectric tensor of the medium as

$$\overleftrightarrow{\varepsilon} = \begin{bmatrix} \varepsilon + \delta\cos 2\beta z & \delta \sin 2\beta z & 0 \\ \delta \sin 2\beta z & \varepsilon - \delta \cos 2\beta z & 0 \\ 0 & 0 & \varepsilon_\perp \end{bmatrix}, \tag{6}$$

where $\varepsilon = (\varepsilon_\parallel + \varepsilon_\perp)/2$ and $\delta = (\varepsilon_\parallel - \varepsilon_\perp)/2$. $\varepsilon_\parallel$ and $\varepsilon_\perp$ are the dielectric constants along the long and short molecular axes, respectively. The above dielectric ellipsoid starts with the long molecular axis pointing in the x-direction at $z = 0$ and spirals with a pitch $P = 2\pi/\beta$ along the z-direction. Maxwell's equations in such a uniaxial medium can be expressed as a set of four linear differential equations for the tangential components of the electric and magnetic fields [59]:

$$\frac{\mathrm{d}\psi}{\mathrm{d}z} = \frac{\mathrm{i}\omega}{c}\overleftrightarrow{\Delta}\,\psi, \tag{7}$$

where $\psi = (E_x, H_y, E_y, -H_x)^{\mathrm{T}}$ and c is the speed of light in vacuum. The matrix $\overleftrightarrow{\Delta}$ has the form

$$\overleftrightarrow{\Delta} = \begin{bmatrix} 0 & 1 - X^2/\varepsilon_\perp & 0 & 0 \\ \varepsilon + \delta\cos 2\beta z & 0 & \delta \sin 2\beta z & 0 \\ 0 & 0 & 0 & 1 \\ \delta \sin 2\beta & 0 & \varepsilon - X^2 - \delta\cos 2\beta z & 0 \end{bmatrix}, \tag{8}$$

where $X = n_{\mathrm{o}} \sin\theta$. The solution of Eq. (7) can be expressed in the form

$$\psi(L) = \overleftrightarrow{Q}(L,0)\psi(0) \quad \text{or} \quad \psi(0) = \overleftrightarrow{Q}^{-1}(L,0)\psi(L), \tag{9}$$

where $\overleftrightarrow{Q}$ is a 4×4 transfer matrix and can be obtained numerically. If we denote ψ_{i} and ψ_{r} as the incident and reflected waves, respectively, at $z = 0$, and ψ_{t} as the transmitted wave at $z = L$, Eq. (9) becomes

$$\psi_{\mathrm{i}} + \psi_{\mathrm{r}} = \overleftrightarrow{Q}^{-1}\psi_{\mathrm{t}}, \tag{10}$$

For plane wave incidence at an angle θ to the z-axis in the $x-z$ plane, we can write $\psi_{\mathrm{i}} = (E_x, \gamma_x E_x, E_y, \gamma_y E_y)$, $\psi_{\mathrm{r}} = (R_x, -\gamma_x R_x, R_y, -\gamma_y R_y)$ and $\psi_{\mathrm{t}} = (T_x, \gamma_x T_x, T_y, \gamma_y T_y)$, where $\gamma_x = n_b/\sin\theta$ and $\gamma_y = n_b \sin\theta$. Here (E_x, E_y), (R_x, R_y), and (T_x, T_y) denote the tangential components of the electric fields for the incident, reflected, and transmitted waves, respectively [59]. For circularly polarized incident light, the electric field components have the forms $E_x = \pm \mathrm{i}E_0 \cos\theta$, $E_y = E_0$ and $E_z = \pm \mathrm{i}E_0 \sin\theta$. Thus, the values of (R_x, R_y), and (T_x, T_y) can be obtained by solving Eq. (10). By using $T_z = T_x \tan\theta$ and $R_z = R_x \tan\theta$, the transmittance and reflectance can be written as $T = (T_y^2 + T_x^2/\cos^2\theta)/E_0^2$ and $R = (R_y^2 + R_x^2/\cos^2\theta)/E_0^2$, respectively.

In order to obtain the transfer-matrix $\overleftrightarrow{Q}$ numerically, the sample is divided into N layers of equal thickness $h = L/N$ and $\overleftrightarrow{Q}$ is expressed as products of the transfer

matrices in each layer, i.e., $\overleftrightarrow{Q} = \prod_{j=1}^{N} P_j$. The dielectric tensor of Eq. (6) is assumed not to change within each layer, say $\overleftrightarrow{\Delta}_j = \overleftrightarrow{\Delta}$ in the jth layer. The formal solution of Eq. (7) for the jth layer then has the form, $\psi(jh) = P_j[jh,(j-1)h]\psi[(j-1)h] = \exp(\mathrm{i}(\omega h/c)\overleftrightarrow{\Delta}_j)\psi[(j-1)h]$. To evaluate the exponential operator P_j in each layer, we use the analytic expression of Wohler et al. obtained by using a theorem due to Cayley and Hamilton [60]. The value of N is increased until the transmittance converges. The final value of h used is always much smaller than the pitch P of the CLC film, or the wavelength at the band edges.

Computer simulation is made of a CLC film of thickness $L = 35\,\mu\mathrm{m}$. The sample has a pitch $P = 370\,\mathrm{nm}$ and dielectric constants $\varepsilon_{\parallel}$ and $\varepsilon_{\perp}$, that correspond to $n_{\parallel} = 1.8$ and $n_{\perp} = 1.6$ for the extraordinary and ordinary refractive indices, respectively. For the background medium, we use $n_{\mathrm{b}} = 1.52$.

The result of the transmittance as a function of vacuum wavelength λ for a normally incident RCP plane wave is shown in Fig. 9 in the region near the band edge. The first peak near the high frequency side of the bandgap is the narrowest one. The transmission spectrum as a function of incident angle at the resonant frequency of the band-edge state, $\lambda = \lambda_{\mathrm{r}}$, is plotted in Fig. 25. The band-edge shifts to higher frequency with increasing oblique angle so that the wave is evanescent over a wide range of angles.

Gain is introduced into the CLC film by adding a small negative imaginary part to both $\varepsilon_{\parallel}$ and $\varepsilon_{\perp}$ in Eqs. (6) and (7). The width of the band-edge state in the transmission spectrum decreases with the increasing gain coefficient and vanishes at the critical gain. At this point, both the transmittance and reflectance diverge. Unlike many conventional lasers based on Fabry-Perot (FP) resonators, the band-edge and defect modes of 1D bandgap structures are significantly narrower than other modes. This leads to the generation of single-frequency radiation when the sample is excited slightly above threshold.

In order to understand the ring structure, we use a finite-sized incident beam, instead of an incident plane-wave. For simplicity of calculation, the incident beam is taken to be a 1D Gaussian wave instead of a Gaussian wave. The main results obtained for a 1D Gaussian wave hold in the case of a Gaussian wave. For an RCP wave, the electric field of a 1D Gaussian wave can be expressed as

$$\vec{E}^{\mathrm{inc}}(x,z) \equiv \begin{pmatrix} E_x(x,z) \\ E_y(x,z) \\ E_z(x,z) \end{pmatrix} = E_0 \int \begin{pmatrix} \cos\theta \\ \mathrm{i} \\ \sin\theta \end{pmatrix} F(\theta) \exp\left(\mathrm{i}\frac{\omega n_b \sin\theta}{c}x\right) \times \exp\left(\mathrm{i}\frac{\omega n_b \cos\theta}{c}z\right) \mathrm{d}\theta \tag{11}$$

with

$$F(\theta) = \frac{1}{\sigma\sqrt{2\pi}} \exp\left(-\frac{\theta^2}{2\sigma^2}\right),$$

where σ is the width of the angular distribution, and $\omega n_b \sin\theta/c$ and $\omega n_b \cos\theta/c$ are the wavevectors in the x- and z-direction, respectively. Thus, the electric field $\vec{E}$ constructed in Eq. (11) is homogeneous in the y-direction and has a Gaussian profile in the x-direction with a minimum width, σ at $z = 0$. For this incident beam, the electric field of the transmitted beam in the region $z \geqslant L$ can be expressed as

$$\vec{E}^{T}(x,z) = \begin{bmatrix} E_x^T(x,z) \\ E_y^T(x,z) \\ E_z^T(x,z) \end{bmatrix} = \int \begin{bmatrix} T_x(\theta) \\ T_y(\theta) \\ T_x(\theta)\tan\theta \end{bmatrix} F(\theta) \exp\left(i\frac{\omega n_b \sin\theta}{c}x\right) \times \exp\left[i\frac{\omega n_b \cos\theta}{c}(z-L)\right] d\theta, \quad (12)$$

where the functions $T_x(\theta)$ and $T_y(\theta)$ are the solutions of Eq. (10). The wave intensity distribution at any plane $z = z_0 \geqslant L$ on the transmitted side, i.e., $I(x, z = z_0) \propto (|E_x^T(x,z_0)|^2 + |E_y^T(x,z_0)|^2 + |E_z^T(x,z_0)|^2)$, is calculated using Eq. (12).

A typical intensity distribution at the output surface $z_0 = L$ for a gain coefficient slightly below the critical value is shown in the linear and logarithmic plots in Fig. 28. The intensity distribution is seen to decay exponentially, $I \propto \exp(-2\alpha|x|)$, at the frequency of the band-edge state for the perpendicularly propagating wave, $\omega = 2\pi c/\lambda_r$. The value of α decreases with increasing gain coefficient and vanishes at the critical gain. The dashed curve in Fig. 28 shows the phase of the electric field. Except in a small region near the center, the phase increases linearly from the center

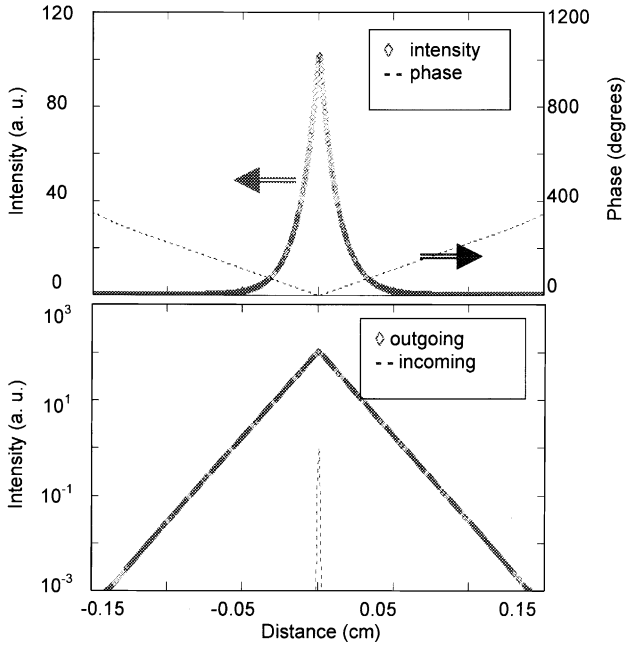

Fig. 28. Computer simulations of spatial distribution of laser emission at output surface of CLC.

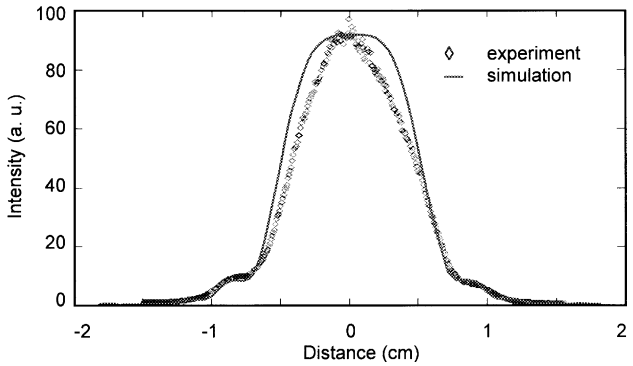

Fig. 29. Comparison of measurements of spatial distribution of laser emission in the far field (11.5 cm from sample) with computer simulations.

with the same coefficient α, i.e., $\phi = \alpha|x|$. These results indicate a wavefunction of the form $\exp[-\alpha(1 - \mathrm{i})|x|]$ at the output surface. The value of α does not depend upon the width of the incident beam.

The far-field intensity distribution at $z_0 - L = 11.5$ cm corresponding to the case of Fig. 28 is shown in Fig. 29 using a linear scale. A ring structure similar to one observed experimentally is clearly seen. The intensity distribution near the peak is now much flatter than on the output surface. Assuming uniform gain in the film, the field on the output surface becomes a plane wave of infinite transverse extent at the critical gain. In practice, the gain region is always bounded and the transmitted wave is limited by the extent of either the gain region or the incident wave and by saturation. For a sample at critical gain, the angular confinement of the wave will produce a ring pattern in the far field. The ring pattern can be observed even for an infinite gain region, but only below the lasing threshold.

The exponential decay of the intensity at the output surface can be understood as follows. The resonant peak of the transmitted wave at the band-edge state has a Lorentzian shape. Therefore, the transmitted electric field amplitudes at the output surface for a normally incident beam near the band-edge state, can be written as,

$$T_\beta(k) \approx \frac{C_\beta}{B - \mathrm{i}(k - k_\mathrm{r})} \quad \beta = x, y, z, \tag{13}$$

where C_β and B are constants, and $k = 2\pi n_\mathrm{b}/\lambda$ and $k_\mathrm{r} = 2\pi n_\mathrm{b}/\lambda_\mathrm{r}$ are the wavevectors in the embedding medium. The value of B determines the linewidth of the transmission spectrum, i.e., $2\Delta\lambda = B\lambda_\mathrm{r}^2/\pi n_\mathrm{b}$. When the gain coefficient γ is slightly below the critical value γ_c, B is proportional to $\gamma_\mathrm{c} - \gamma$ and the linewidth vanishes at the critical gain. Eq. (13) can be generalized to include oblique incident waves if we replace k by $k\cos\theta$. At the band-edge frequency $k = k_\mathrm{r}$, the transmittance is strongly peaked in the normal direction. In the limit $B \ll k_\mathrm{r}, \cos\theta \gg 1 - \theta^2/2$, and Eq. (13) gives

$$T_\beta(\theta, k = k_\mathrm{r}) \approx \frac{2C_\beta}{2B + \mathrm{i}\theta^2 k_\mathrm{r}}. \tag{14}$$

By substituting Eq. (14) into Eq. (12) and using the fact that Eq. (14) is a strongly peaked function at $\theta = 0$, we find

$$E_\beta^{\mathrm{T}}(x, z = L) \cong 2F(0)C_\beta \int \frac{1}{2Bk_\mathrm{r} + \mathrm{i}(\theta k_\mathrm{r})^2} \exp(\mathrm{i}k_r\theta x)\, \mathrm{d}(\theta k_\mathrm{r}). \tag{15}$$

Straightforward integration leads to

$$E_\beta^{\mathrm{T}}(x, z = L) \propto \exp[-(1-\mathrm{i})\sqrt{Bk_\mathrm{r}}|x|]. \tag{16}$$

This is the field plotted in Fig. 28 with $\alpha = \sqrt{Bk_\mathrm{r}}$. The field distribution obtained in Eq. (16) depends only on Bk_r and is independent of the spatial extent of the incident beam. Since B is proportional to $\gamma_\mathrm{c} - \gamma$, the wavefunction becomes a plane wave of infinite extent as the gain approaches its critical value. It should be pointed out that Eqs. (15) and (16) become invalid when $|x| \ll 1/\sqrt{Bk_\mathrm{r}}$. In this limit, higher order terms in θ^2 cannot be neglected in the denominator of the integrand in Eq. (15).

The width of the beam can be defined to be $W \equiv 2x_0$ where x_0 is the position at which the intensity drops to half of its peak value. From Eq. (16), this gives a beam width at the output surface of $W = \ln 2/\sqrt{Bk_\mathrm{r}}$. Substituting $2\Delta\lambda = B\lambda_\mathrm{r}^2/\pi n_\mathrm{b}$ and $k_\mathrm{r} = 2\pi n_\mathrm{b}/\lambda_\mathrm{r}$ into the previous relation gives a universal relation between W and the linewidth in transmission of normally incident radiation, $2\Delta\lambda$ at λ_r,

$$\frac{\lambda_\mathrm{r}}{n_\mathrm{o} W} = \frac{\sqrt{2}\pi}{\ln 2}\sqrt{\frac{2\Delta\lambda}{\lambda_\mathrm{r}}}. \tag{17}$$

This relation is valid as long as $B \ll k_\mathrm{r}$. This condition is satisfied when the gain coefficient is sufficiently close to the critical value. It can also be reached in the absence of gain when the sample is sufficiently thick. Since it does not explicitly depend on characteristics of the sample, this relation also holds for lasing modes in other layered media, such as BL media and FP resonators. This is demonstrated in Fig. 30, where we plot $\lambda_\mathrm{r}/n_0 W$ vs. $\Delta\lambda/\lambda_r$ on a log-log scale for three systems: (a) CLC ($\diamond$), (b) BL ($+$), (c) FP (x). Eq. (17) is plotted as a solid line for comparison. Results are also presented for two CLC samples with different thickness ($\square$) in the absence of gain.

Since the linewidth in the transmission spectrum is inversely proportional to the dwell time τ of the wave in the sample, Eq. (17) can be interpreted as a diffusion relation:

$$W^2 \sim D\tau. \tag{18}$$

Eq. (17) can be rewritten in a more elegant way as

$$W^2 = (\ln 2)^2/(k_\mathrm{r}\Delta k_\mathrm{r}). \tag{19}$$

By using $\tau \sim (\Delta\omega)^{-1} = n_\mathrm{b}/(c\Delta k_r)$, we find the effective diffusion constant

$$D = c/(n_b k_\mathrm{r}), \tag{20}$$

which is proportional to the wavelength of the lasing mode. Quite surprisingly, it is independent of sample thickness, gain coefficient or index contrast. This diffusion-like result can be seen more directly from the pole of the transmission amplitude in

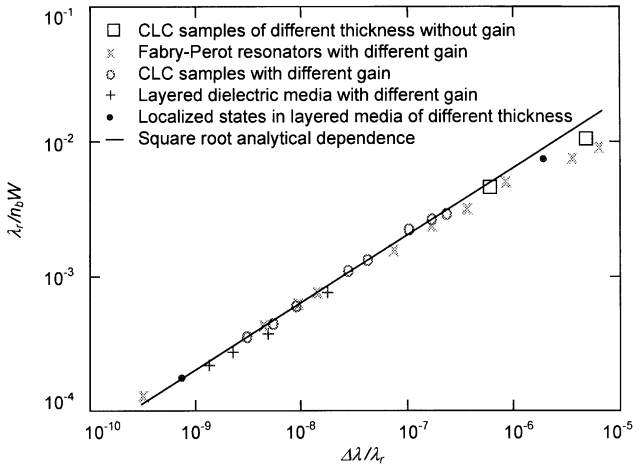

Fig. 30. Comparison of the universal relation for the dependence of the inverse beam width upon relative linewidth of Eq. (9), shown as solid line, with simulations of transmission at the band edge of CLC (○) and BL (+) systems and in FP (x) systems with different values of gain, through CLC samples of different thickness (□), and at localized states in the middle of the bandgap of BL (●) samples of different thickness.

Eqs. (14) and (15). In the small θ limit, $\theta\, k_r$ is the transverse wavevector, k_x. Apart from a constant of proportionality, the pole can be expressed in diffusion form, $-i\Delta\omega + Dk_x^2$, where $\Delta\omega/D = 2Bk_r$. By using $2\Delta\lambda = B\lambda_r^2/\pi n_b$ and $\Delta\omega \sim 1/\tau$, we recover $D \sim \lambda_r$.

Although the incident wave was assumed to be homogeneous in the y-direction, this condition can easily be relaxed. If the incident beam is a Gaussian wave in both the x- and y-direction, the immediate generalization of Eq. (15) gives

$$E_\beta^T(x, y; z = L) \propto \iint \mathrm{d}k_x\, \mathrm{d}k_y \frac{1}{2Bk_r + i(k_x^2 + k_y^2)} \exp(ik_x x)\exp(ik_y y). \tag{21}$$

The above integral is the Fourier transform of a 2D diffusive pole. The solution is an outgoing wave from a point source at the origin, i.e., $E_\beta^T(x, y; z = L) \propto H_0^1[(1+i)\sqrt{Bk_r}\rho]$, where H_0^1 is a Hankel function and $\rho = \sqrt{x^2 + y^2}$. Eq. (18) becomes invalid when $\rho \ll 1/\sqrt{Bk_r}$. For $\rho \gg 1/\sqrt{Bk_r}$, we find $E_\beta^T \propto (1/\sqrt{\rho})\exp[-(1-i)\sqrt{Bk_r}\rho]$. This is similar to the field distribution found in Eq. (16) and gives rise to the ring structure observed experimentally for excitation slightly above the lasing threshold.

5.4. Diffusion of coherence

Because of the upward shift of the edge of a stop band in 1D periodic structures with increasing oblique angle, only a single mode of radiation at the frequency of the first mode can propagate over a wide angular range centered about the normal direction. As a result, the transmitted light or lasing emission at this frequency has a

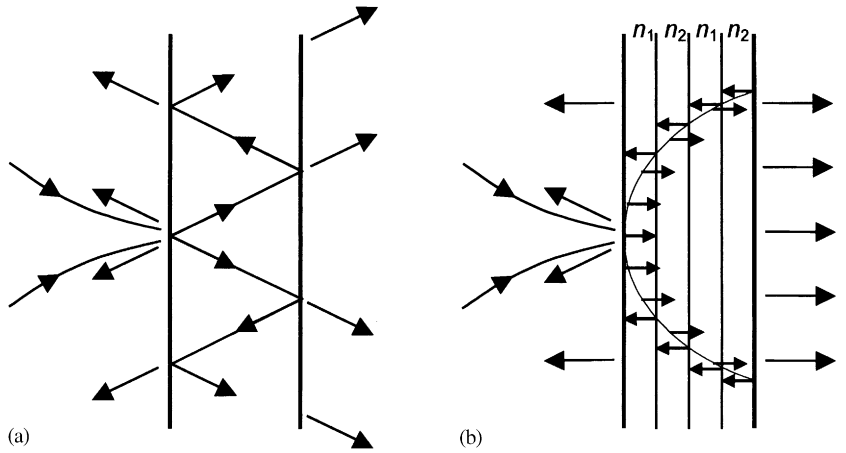

Fig. 31. Coherent spreading of beam inside an amplifying medium. (a) Two flat mirrors define a cavity, in which spreading of the beam involves oblique wavevector components. The resulting beam size is linearly proportional to the photon dwell time. (b) Layered photonic band-gap medium, in which oblique components of the wavevector are reflected, since their propagation falls within the stop band, except for wavevector component close to the normal. The beam width is proportional to the square root of the photon dwell time.

wide exponential spatial distribution with a width that may be considerably greater than the sample thickness. The width of the transmitted spatial distribution varies inversely with the linewidth of the transmitted light. This corresponds to a narrow divergence and to a ring pattern in the transmitted beam. The spread of coherent radiation inside a 1D photonic structure is completely different from that in a FP resonator (Fig. 31). In the latter case (Fig. 31a), the spread is associated with oblique components of radiation. A more rapid spread of coherence requires more oblique propagation. The opposite situation obtains in the periodic structure in Fig. 31b, in which the spread occurs due to reflection of oblique components.

6. Chiral twist defect

6.1. Defects in periodic media

We now consider defects in chiral structures. The important role of photonic defects has been understood from the very beginning of the investigation on PCs. Defects in photonic structures can serve for example as perfect lossless waveguides or as long-lived laser cavities [3,61]. Many types of defect have been studied in 1, 2, and 3D isotropic photonic structures. These can be produced by removing or adding material or by altering the refractive index of one or a number of elements in 1, 2, or 3D PCs. Introducing a quarter-wavelength space in the middle of a layered isotropic 1D sample produces a defect in the middle of the reflection band (Fig. 32a). Such a defect is widely used to produce high-Q laser cavities in VCSELs [18].

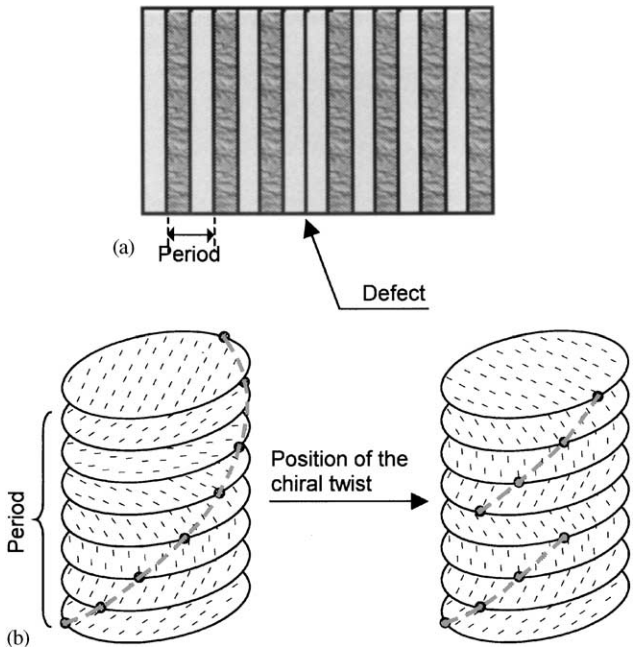

Fig. 32. Schematic of defects in periodic structures. (a) Defect in BL structure. (b) Chiral twist defect produced in periodic cholesteric structure by twisting the top of sample relative to the bottom. Unmodified structure is shown on the left.

In analogy with isotropic periodic structures, a defect can be produced in a helical structure by adding an isotropic layer in the middle of a CLC [62]. The reflections of radiation with opposite senses of circular polarization were shown to be equal at resonance. In addition, a "chiral twist" defect created by rotating one part of the sample about its helical axis without separating the two parts was proposed (Fig. 32b) [63]. Modifying the chiral twist angle from 0° to 180° tunes the defect frequency from the low to the high frequency band edge. A 90° twist produces a photonic defect with a frequency at the center of the stop band. Recently, such a spacerless defect has been created in STFs [64]. A morphological discontinuity was introduced by rotating the substrate by an additional 90° in the middle of the fabrication process. The defect has also been probed in a macroscopic model of a chiral structure constructed from overhead transparency films [65]. Microwave transmission in these structures will be discussed below following a discussion of simulations of propagation through a defect in a chiral medium.

6.2. *Modeling and simulations*

We consider the results of scattering and transfer matrix calculations for the 90° chiral twist defect [66]. The chiral twist defect introduces a single localized mode into the bandgap with a polarization with the same handedness as the structure. In

contrast, an additional spacing introduced into isotropic periodic structures creates a degenerate pair of modes. As a result, the polarization of the chiral twist defect mode is independent of the polarization of the exciting mode, whereas the polarization of the wave inside a 1D isotropic system always matches that of the exciting radiation. The localized chiral defect mode gives rise to a crossover in the nature of propagation. Below a crossover thickness, L_{co}, the localized mode is excited most efficiently by a wave with the same handedness as the structure and exhibits an exponential spatial distribution of the energy density inside the sample and a peak in transmission at the defect frequency (Fig. 33a). Above the crossover, however, the defect mode is only effectively excited by the oppositely polarized wave and a resonant peak appears in reflection (Fig. 33b). Though the polarization is transformed within the sample, the polarization of the transmitted and reflected waves is the same as that of the incident wave.

The energy density inside a right-handed CLC sample is decomposed into components of different circular polarization and propagation direction. We obtain the same results from both scattering [35] and transfer matrix [56] approaches for short structures. For thick structures, the transfer matrix approach becomes unstable and we therefore used the scattering matrix method exclusively. The indices of refraction of the sample are taken to be $n_o = 1.52$ and $n_e = 1.58$. The sample is not absorbing and is nearly index matched to its surroundings, which has a background index of refraction $n_b = n \equiv (n_o + n_e)/2 = 1.55$. The sample pitch is $P = 400\,\text{nm}$, placing the center of the bandgap at vacuum wavelength $\lambda_c = nP = 620\,\text{nm}$.

With a chiral twist of 90° at its physical center, a distinct peak appears in transmission for RCP radiation at λ_c for $L < L_{co}$ (Fig. 33a). The crossover in propagation is seen in simulations of transmission of RCP and reflection of LCP radiation versus structure thickness at the frequency of the localized state (Fig. 34). Fig. 33b shows the disappearance of the peak in transmission for RCP light and the growth of a peak in reflection for LCP light, as well as a narrowing of the resonant

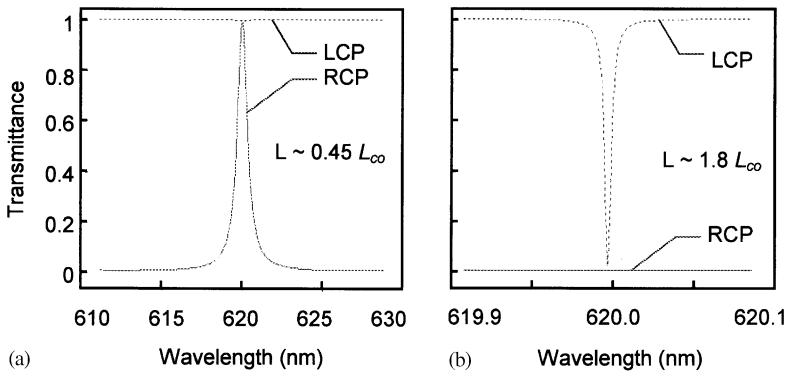

Fig. 33. Transmittance of right and left circularly polarized light versus wavelength for different structure thickness. (a) Structure thickness is less than crossover thickness ($\sim 0.45\,L_{co}$) and (b) structure thickness is bigger than crossover thickness ($\sim 1.8\,L_{co}$).

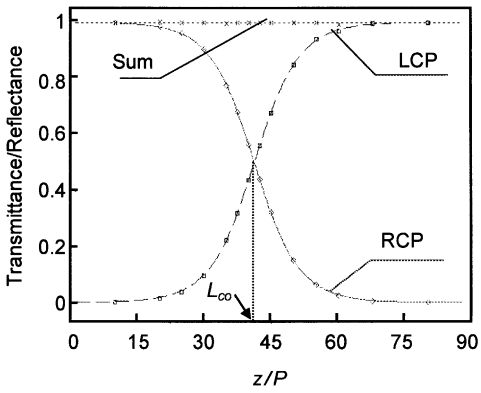

Fig. 34. Transmittance of right and reflectance of left circularly polarized light versus structure thickness in units of the structure pitch P at the defect wavelength.

linewidth as L increases from $0.45L_{co}$ to $1.8L_{co}$. The chiastic variation of transmittance and reflectance at the resonant peak with thickness is displayed in Fig. 34. The crossover thickness, defined as the thickness at which resonant transmission and reflection equal 0.5, is seen in the plot in Fig. 34 and found to be $L_{co} = 41.25P$. The sum of the transmission coefficient of RCP light and the reflection coefficient of LCP light is shown as the dotted line in Fig. 34 and seen to equal unity. At a given thickness, resonant transmission for RCP and LCP light are equal as are the reflection for both polarizations.

The crossover behavior of transmission and reflection at the chiral twist defect resonance can be better understood by considering the spatial distribution of energy inside the sample, shown in Figs. 35 and 36. The energy density of the forward propagating wave inside the structure is shown in Fig. 35 for RCP and LCP radiation in samples with different thicknesses, but for the refractive indices given above. The results are presented for samples of thickness 10, 20, 40, 80 and $160P$, which can be distinguished in the figure by the terminal value of the thickness for each of the curves. At all thicknesses, the intensity reaches a local maximum at the defect site in the middle of the sample. For $L \ll L_{co}$, the intensity falls exponentially from the physical center of the sample for the incident RCP wave, as would occur for a defect in an isotropic medium, while the intensity for incident LCP light is constant throughout the sample. Thus only the incident RCP wave couples to the localized state. This coupling is the cause of the nearly complete transmission of the RCP wave. Since the spatially integrated intensity for the incident RCP wave at resonance scales exponentially, the photon dwell time within the sample does as well. This leads to an exponential increase in the inverse linewidth seen in Fig. 37. For $L \geqslant L_{co}$, the intensity for an incident RCP wave falls at first, then reaches a plateau and then rises to a local maximum in the center of the sample, as seen in Fig. 35. In this case, the value of the local maximum is of the order of or even smaller than the intensity of the incident wave. This indicates that the external RCP wave and the localized mode become decoupled beyond the crossover. In contrast, the intensity for the incident

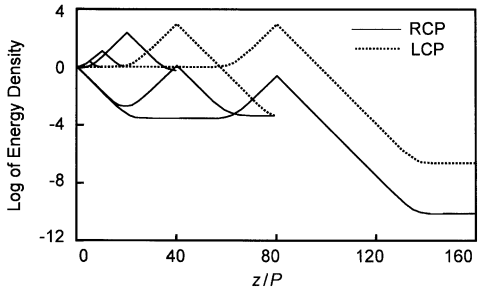

Fig. 35. Energy density of the forward propagating wave inside the structure for different polarizations of the incident wave and sample thickness. The end of each curve corresponds to the structure thickness. P is the structure pitch.

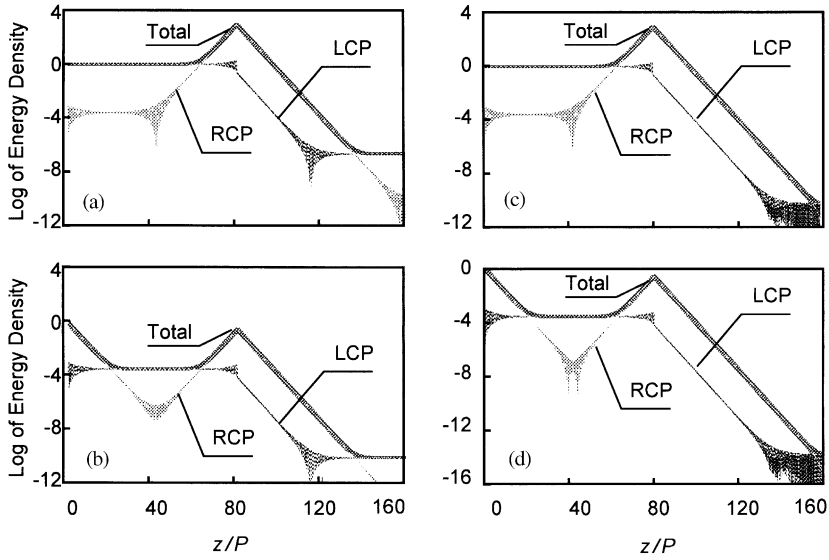

Fig. 36. Energy density inside the structure. (a) and (b) Decomposition of the forward propagating wave into right and left circularly polarized component for left (a) and right (b) circularly polarized incident wave. (c) and (d) Decomposition of the backward propagating wave into right and left circularly polarized component for left (c) and right (d) circularly polarized incident wave.

LCP wave remains at the incident level when first entering the sample and then rises exponentially towards the defect site. Because the rise of intensity for an incident LCP wave occurs deeper into the sample, transmission is small, even though the intensity at the defect is greatly enhanced. The enhancement of intensity by more than three orders of magnitude, shown in Fig. 35, leads to a narrow mode linewidth. Thus the external LCP wave is strongly coupled to the localized mode. This results in weak transmission and strong reflection of the LCP wave. Hence, the reflection of the LCP wave, as well as the transmission of the RCP wave, is the result of coupling

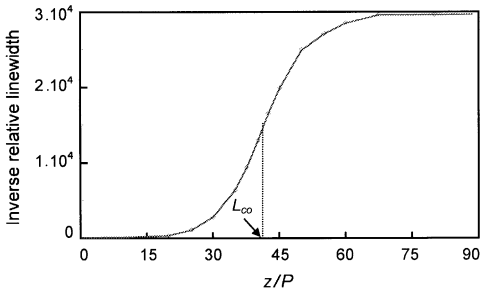

Fig. 37. Inverse relative linewidth ($\lambda_c/\Delta\lambda$) versus sample thickness in units of the pitch P.

to the localized state. Beyond L_{co}, the peak intensity inside the structure, as well as the mode linewidth, which is the same in reflection and transmission, saturates (Fig. 37).

In order to examine the polarization of the defect mode, we decompose the wave inside the medium into two circular polarized components for incident LCP (Figs. 36a and c) and RCP (Figs. 36b and d) waves in a sample with thickness $L = 160P \approx 4L_{co}$. For each polarization of the incident wave, the components propagating in the forward (Figs. 36a and b) and backward (Figs. 36c and d) directions are shown. This makes it possible to see the way in which transmittance and reflectance are related to the excitation of the localized state.

For any sample thickness and for both senses of circular polarization of the exciting radiation, the wave near the defect is RCP and the wave intensities for the two directions of propagation are equal (Figs. 36a–d). Thus, the defect mode is a standing RCP wave near the defect, where most of the energy is stored. Closer to the boundaries, however, the wave is in general elliptically polarized. Decomposing that elliptical wave into its RCP and LCP components, we obtain the coupling coefficient of the mode to RCP or LCP waves external to the sample. The sum of the corresponding coupling coefficients for the energy is therefore unity for any L. The sum of the transmission of RCP and reflection of LCP should therefore also be unity as is seen to be the case in Fig. 34. This suggests that at a given thickness there are two mutually orthogonal elliptically polarized waves. One is completely uncoupled from the localized state and cannot excite it, whereas the other efficiently excites the localized state and determines the polarization of the emission from the structure at the defect frequency. Let us consider the coupled waves at three values of L. For $L \ll L_{co}$, the incoming mode that excites the localized mode is a circularly polarized wave with the same handedness as the structure, RCP in our case. The orthogonal LCP wave does not excite the localized state. At $L = L_{co}$, the localized mode is most efficiently excited by a linearly polarized wave. The perpendicularly polarized wave does not excite the localized state, as seen in Fig. 38. For $L \gg L_{co}$, the wave that couples to the localized state has circular polarization opposite to the handedness of the structure (LCP in our case), while the orthogonal wave, (RCP) does not excite the localized mode.

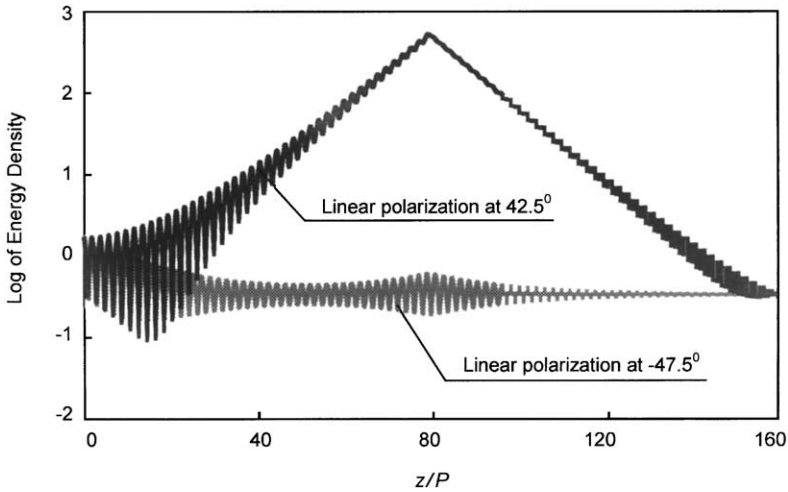

Fig. 38. Total energy density (not just the forward propagating component) inside the structure with thickness of L_{co}. Calculations are made at the resonant frequency for two orthogonal linearly polarized incoming waves, one of which does and the other of which does not couple to the localized mode.

It is interesting to note that for $L \gg L_{co}$ the polarization of the exciting wave at resonance is preserved in reflection, even though it may be efficiently converted to the opposite polarization inside the sample. For example, Fig. 36a and c show that an incident LCP wave is converted to an RCP wave near the defect ($L \sim 80P$) and converted back to an LCP wave near the input boundary ($L < 40P$). Instead of scaling exponentially, the intensity at the site of the localized mode saturates. Nonetheless, the intensity enhancement can be greater than 10^3 as is seen in Fig. 36. This gives a resonant Q-factor of more than 30,000. Much larger values of Q are calculated for structures with lower anisotropy. Achieving such Qs requires the development of highly periodic structures with chiral symmetry such as STFs or polymeric CLCs. This would open the way for a variety of active and passive integrated polarization sensitive devices including low-threshold lasers. It would be of particular interest to produce an electronically excited gain region at the site of the defect between two chiral layers to achieve an organic analog of a VCSEL.

6.3. *Optical and microwave measurements*

Hodgkinson et al. [64] created a 90° chiral twist defect within a chiral structure by an additional rotation of the substrate in the middle of the fabrication process. The measured transmittance (Fig. 39a) is in good agreement with computer simulation for this structure (Fig. 39b).

Both the average index n and the anisotropy of the structure Δn depend upon the index of the porous region between the columns. The optical transmittance of a structure permeated with a liquid may therefore serve as a sensitive probe of the

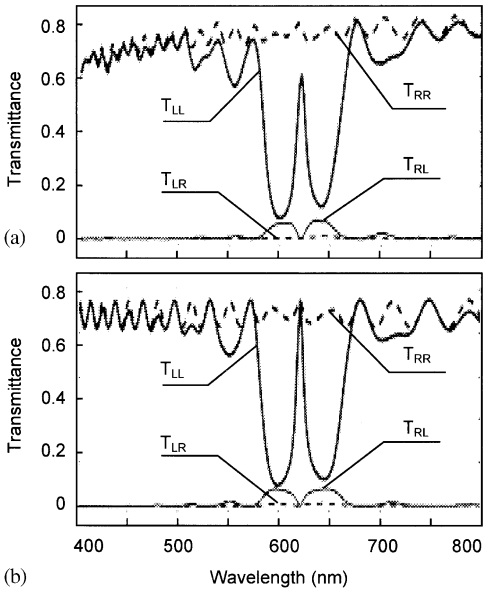

Fig. 39. Measurements (a) and simulations (b) of transmittance spectra of two left-handed STF with 90° chiral twist. (adapted from Ref. [64]).

molecular concentration. Gain may be introduced into such structures by soaking the structure with dye solution.

We have created a model sample with the symmetry of a CLC by stacking Highland 701 transparency films of thickness 0.11 mm with a fixed angle between successive sheets [65]. The pitch of the right-handed structure is 88 transparencies equal to 9.6 mm, giving a rotation angle of 4.09° between transparencies. The transparencies stack is right handed. The transparencies are held in a plastic structure consisting of a base plate connected by rods to a top with a wide centered hole as illustrated in Fig. 40. Nylon fishing lines are threaded between the two plates to create a cylindrical retainer and a guide for rotating successive transparencies by placing the corner of each transparency between two fishing lines. The entire structure is then placed within a box with absorbing sides with 10-cm diameter holes on the top and the bottom.

A Hewlett Packard 8722 vector network analyzer is used to measure the spectrum of the transmitted microwave field. The microwave source is a horn that emits elliptically polarized light and is readily adjusted to emit RCP, LCP, or linearly polarized radiation. The horn is placed with its opening in the center of the bottom of the box. The receiver horn is hung about four feet above the hole in the top of the box using fishing lines.

The indices of refraction for light propagating perpendicular to the plane of the transparencies and polarized along and perpendicular to the length of the transparencies are $n_{\parallel} = 1.838$ and $n_{\perp} = 1.782$, respectively. These values are

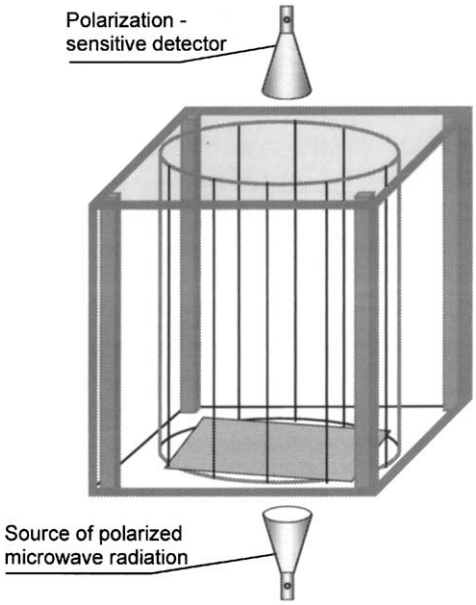

Fig. 40. Microwave setup.

obtained by measuring the microwave phase accumulated in propagating through a stack of 10 aligned transparencies without rotation between successive sheets. The absorption coefficient for the transparencies is found to be $\alpha = 0.017\,\mathrm{cm}^{-1}$ from measurements of transmission of LCP radiation versus the number of sheets in a right-handed stack.

The first sample studied consisted of 1,500 transparencies to form a structure with CLC symmetry as described above. The amplitude of the transmitted field is squared to give the intensity spectra. The intensity spectrum for transmitted RCP radiation from an RCP source is normalized to that for the transmitted LCP wave obtained for an LCP source. The results seen in Fig. 41 are in close correspondence to simulations for infinite CLC sheets carried out using the measured indices of the birefringent transparency films.

Next a 90° chiral twist defect is created by adding a similar stack of 1500 sheets with right-handed CLC symmetry in which the first transparency of the second stack is rotated by an additional 90° relative to the sheet on the top of the first stack. The transmission spectrum for the RCP wave normalized to that for the LCP wave is shown in Fig. 42. A peak in transmission appears in the middle of the gap at resonance with the localized state. A simulation of transmission for infinite sheets is also shown in the figure. The measured spectrum shown in the figure is broadened and shifted to wavelengths shorter than the central wavelength of the gap at which the transmission peak is found in the simulation. When the measured absorption is included in the simulation, the transmission peak is reduced and the line broadens, but remains in the center of the stop band. A natural explanation of the additional

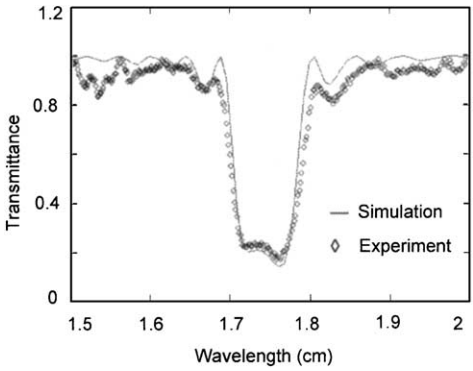

Fig. 41. Transmittance through stack of 1500 transparencies.

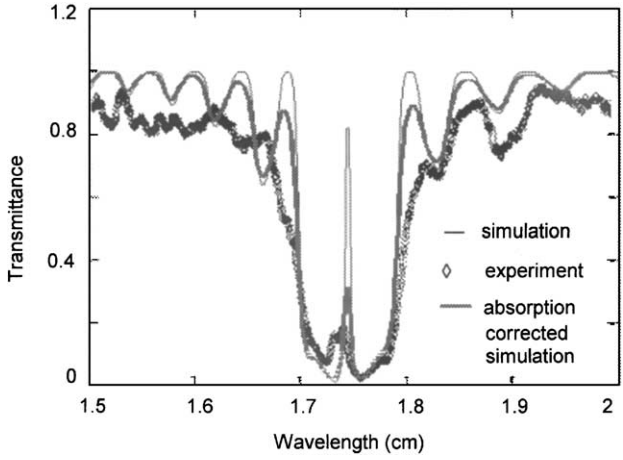

Fig. 42. Transmittance through stack of 3000 transparencies with a 90° chiral twist defect in the middle.

broadening and shift of the line is the presence of an angular spread in the waves launched and detected in this experiment. Simulations of transmission for an oblique incident plane wave show a shift towards shorter wavelength with increasing angle of incidence. The horns used had an effective aperture of $\sim$4 cm, giving a 30° acceptance angle for microwave radiation at the frequency of the defect mode. The transmission spectrum for an absorbing sample with a 90° chiral twist is calculated for a Gaussian angular distribution with a standard deviation of 15°. Taking into account the angular spread of the incident beam gives improved agreement with experiment, as is seen in Fig. 43. The localized mode is broadened as a result of the spectral shift of oblique components of the incident wave to the short wavelength side. In addition, this angular shift causes the first mode at the short wavelength band edge to be washed out in contrast to the well-defined first mode observed at the

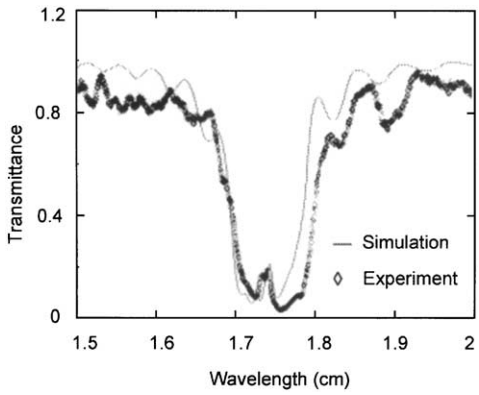

Fig. 43. Transmittance through a stack of 3000 transparencies with a 90° chiral twist defect in the center. Both the angular spread and absorption are taken into account in the simulation.

long wavelength edge. The mode at the long-wavelength edge is clearly discerned because oblique components contribute to the transmission in the frequency range of the stop band for normally incident radiation. This contrasts with transmission near the first mode at the short wavelength edge where oblique components fall into the stop band.

Next, the transmission through a 45° chiral twist defect in the middle of two stacks of 1500 transparencies was measured. The measured spectrum, as well as a simulation for normally incident radiation, which takes account of absorption, is shown in Fig. 44. Finally, we measured transmission in a defect that is a combination of a chiral twist and spacer. The defect in the middle of two stacks of 1500 transparencies consists of a $\lambda/8$ spacer consisting of 11 transparencies stacked without rotation followed by a $-45°$ chiral twist. The net result is equivalent to introducing a single $\lambda/4$ spacer into the structure, which has a defect wavelength in the middle of the stop band. The result is shown in Fig. 45. Including the angular spread of the incident wave improves agreement with experimental results shown in Figs. 44 and 45, as was the case for the 90° chiral twist defect discussed above.

6.4. Discussion

The necessity to include the angular distribution in transmission at resonance with the localized state in simulations in order to provide agreement with microwave measurements indicates that, even in stacks only as thick as 34 times the pitch, the spread of coherence within the sample at resonance can be significant. Simulations of transmission within the stop band are found to agree with measurements, even without accounting for the angular spread and absorption. This is because the spread of coherence and loss of energy due to absorption is limited by the short photon dwell time of the evanescent wave.

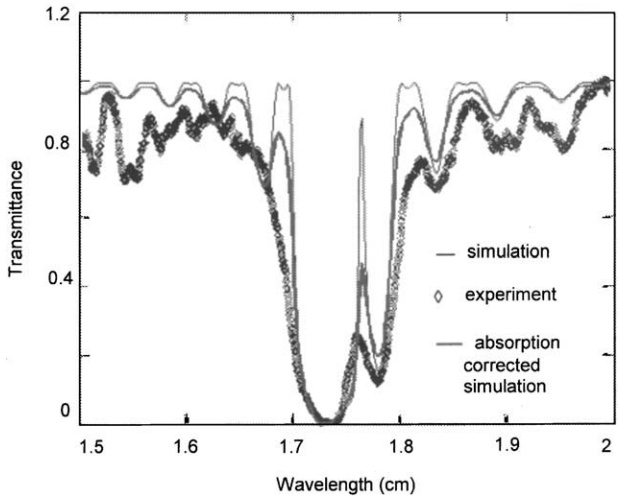

Fig. 44. Transmittance through a stack of 3000 transparencies with a 45° chiral twist defect in the center.

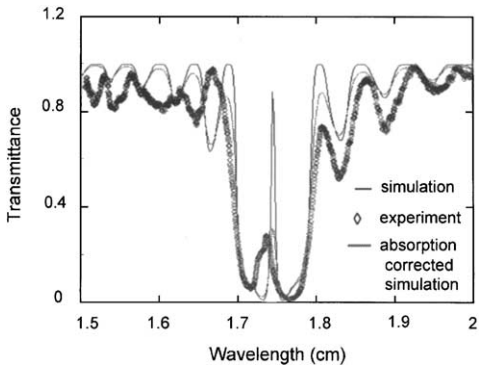

Fig. 45. Transmittance through a stack of 3000 transparencies, with a combination of a 45° rotation and a quarter- wavelength separation in the center.

7. Conclusion

There has been rapid progress in recent years in the development of PCs as tools for manipulating the density of photonic states. The rate of spontaneous emission is proportional to the DOS. Thus emission is suppressed within the PBG, while it is enhanced at specific frequencies corresponding to extended modes at the band edge or localized modes with the bandgap. Though the DOS is strongly suppressed only in a full 3D PBG, the DOS of waves propagating in a specific direction can be significantly enhanced in two or even in one-dimensional photonic structures. This corresponds to an enhanced photon dwell time and facilitates low-threshold lasing in that direction.

Here, we have considered photonic and lasing properties of anisotropic 1D periodic structures with chiral symmetry. In these structures, the DOS is only modified for light waves of a specific polarization. At resonance with either band-edge or localized modes, the coherence area of the wave spreads as a consequence of the angular selectivity of long-lived isolated modes. This makes possible coherent lasing over a length scale that may greatly exceed the structure thickness.

The inherent continuity of chiral structures naturally allows their fabrication by a continuous deposition process as in the case of STFs or as self-organized structures as is the case of CLCs. The combination of frequency and polarization selectivity in chiral photonic structures facilitates lasing in a single polarized mode. The suppression of wavelength-scale modulation in the standing circularly polarized localized or band-edge mode largely eliminates spatial holeburning and thereby enhances the stability of chiral lasers.

Acknowledgements

We thank Peter Shibaev, Jon Singer, Yury Yarovoy, and Dan Neugroschl of Chiral Photonics and Ranojoy Bose of Queens College. We gratefully acknowledge the support of the NSF (DMR9973959) and ARO (DAAD19-00-1-0362) in carrying out this research.

References

[1] V.P. Bykov, Soviet Physics JETP 35 (1972) 269;
V.P. Bykov, Soviet Physics—Doklady 17 (1973) 658.
[2] E. Yablonovitch, Physical Review Letters 58 (1987) 2059.
[3] J.D. Joannopoulos, R.D. Meade, J.N. Winn, Photonic Crystals: Molding the Flow of Light, Princeton University Press, Princeton, NJ, 1995.
[4] C.M. Soukoulis, (Ed.), Photonic Band Gaps and Localization, NATO ASI Series B: Physics, Vol. 308, Plenum, New York, 1993.
[5] C.M. Soukoulis, (Ed.), Photonic Band Gaps and Localization, NATO ASI Series E: Applied Sciences, Vol. 315, Kluwer Academic, Dordrecht, The Netherlands, 1996.
[6] C.M. Soukoulis, (Ed.), Photonic Crystals and Light Localization in the 21st Century, NATO ASI Series C: Mathematical and Physical Sciences, Vol. 563, Kluwer Academic, Dordrecht, The Netherlands, 2001.
[7] A. Adibi, A. Scherer, S.-Y. Lin, (Eds.), Photonic Bandgap Materials and Devices, Proceedings of the SPIE International Society of Optical Engineering 4655 (2002).
[8] V.N. Astratov, Yu.A. Vlasov, O.Z. Karimov, A.A. Kaplyanskii, Yu.G. Musikhin, N.A. Bert, V.N. Bogomolov, A.V. Prokofiev, Physics Letters A 222 (1996) 349.
[9] K.M. Ho, C.T. Chan, C.M. Soukoulis, Physical Review Letters 65 (1990) 3152.
[10] E. Yablonovitch, T.J. Gmitter, K.M. Leung, Physical Review Letters 67 (1991) 2295.
[11] P. Etchegoin, Physical Review E 62 (2000) 1435.
[12] W. Cao, A. Mucoz, P. Palffy-Muhoray, B. Taheri, Nature Materials 1 (2002) 111.
[13] K. Busch, S. John, Physical Review E 58 (1998) 3896.
[14] A. Blanco, E. Chomski, S. Grabtchak, M. Ibisate, S. John, S.W. Leonard, C. Lopez, F. Meseguer, H. Miguez, J.P. Mondia, G.A. Ozin, O. Toader, H.M. van Driel, Nature 405 (2000) 437.
[15] J.P. Dowling, M. Scalora, M.J. Bloemer, C.M. Bowden, Journal of Applied Physics 75 (1994) 1896.

[16] M.D. Tocci, M. Scalora, M.J. Bloemer, J.P. Dowling, C.M. Bowden, Physical Review A 53 (1996) 2799.
[17] V.I. Kopp, B. Fan, H.K.M. Vithana, A.Z. Genack, Optical Letters 23 (1998) 1707.
[18] H. Yokoyama, K. Ujihara, (Eds.), Spontaneous Emission and Laser Oscillation in Microcavities, CRC Press, Boca Raton, FL, 1995.
[19] O. Painter, R.K. Lee, A. Scherer, A. Yariv, J.D. O'Brien, P.D. Dapkus, I. Kim, Science 284 (1999) 1819.
[20] A. Mekis, J.C. Chen, I. Kurland, S. Fan, P.R. Villeneuve, J.D. Joannopoulos, Physical Review Letters 77 (1996) 3787.
[21] S.Y. Lin, E. Chow, V. Hietch, P.R. Villeneuve, J.D. Joannopoulos, Science 282 (1998) 274.
[22] S. Noda, A. Chutinan, M. Imada, Nature 407 (2000) 608.
[23] J.C. Knight, J. Broeng, T.A. Birks, P.St.J. Russell, Science 282 (1998) 1476.
[24] M. Scalora, J.P. Dowling, C.M. Bowden, M.J. Bloemer, Physical Review Letters 73 (1994) 1368.
[25] W. Chen, D.L. Mills, Physical Review Letters 58 (1987) 160.
[26] D.L. Mills, S.E. Trullinger, Physical Review B 36 (1987) 947.
[27] D.N. Christodoulides, R.I. Joseph, Physical Review Letters 62 (1989) 1746.
[28] S. John, N. Aközbek, Physical Review Letters 71 (1993) 1168.
[29] S.F. Mingaleev, Y.S. Kivshar, Physical Review Letters 86 (2001) 5474.
[30] E. Centeno, D. Felbacq, Physical Review B 62 (2000) R7683.
[31] M. Scalora, M.J. Bloemer, A.S. Manka, J.P. Dowling, C.M. Bowden, R. Viswanathan, J.W. Haus, Physical Review B 56 (1997) 3166.
[32] J.P. Dowling, C.M. Bowden, Physical Review A 46 (1992) 612.
[33] J.M. Bendickson, J.P. Dowling, M. Scalora, Physical Review E 53 (1996) 4107.
[34] S. Yang, J.H. Page, Z. Liu, M.L. Cowan, C.T. Chan, P. Sheng, Physical Review Letters 88 (1–4) (2002) 104301.
[35] V.I. Kopp, A.Z. Genack, Proceedings of the SPIE 3623 (1999) 71.
[36] M.C. Mauguin, Bulletin de la Societe Francaise de Mineralogie et de Cristallographie. 34 (1911) 71.
[37] C.W. Oseen, Transactions of the Faraday Society 29 (1933) 883.
[38] H. de Vries, Acta Crystallographica 4 (1951) 219.
[39] S. Chandrasekhar, Liquid Crystals, Cambridge University Press, Cambridge, 1977.
[40] C. Elachi, C. Yeh, Journal of the Optical Society of America 63 (1973) 840.
[41] R. Dreher, G. Meier, A. Saupe, Molecular Crystals and Liquid Crystals 13 (1971) 17.
[42] P.A. Bermel, M. Warner, Physical Review E, 65 (2002) 056614.
[43] K. Robbie, D.J. Broer, M.J. Brett, Nature 399 (1999) 764.
[44] A. Lakhtakia, R. Messier, Optics & Photonics News, September 2001, 27.
[45] Q. Wu, I.J. Hodgkinson, A. Lakhtakia, Optical Engineering 39 (2000) 1863.
[46] S.H. Chen, D. Katsis, A.W. Schmid, J.C. Mastrangelo, T. Tsutsui, T.N. Blanton, Nature 397 (1999) 506.
[47] L.S. Goldberg, J.M. Schnur, US Patent 3,771,065, 1973.
[48] I.P. Il'chishin, E.A. Tikhonov, V.G. Tishchenko, M.T. Shpak, JETP Letters 32 (1981) 27.
[49] H. Kogelnik, C.V. Shank, Journal of Applied Physics 43 (1972) 2327.
[50] P. Il'chishin, A.Yu. Vakhnin, Molecular Crystals and Liquid Crystals 265 (1995) 687.
[51] A. Muñoz, P. Palffy-Muhoray, B. Taheri, Optics Letters 26 (2001) 804.
[52] S. John, T. Quang, Physical Review Letters 74 (1995) 3419.
[53] S. John, Physical Review Letters 58 (1987) 2486.
[54] H. Finkelmann, S.T. Kim, A. Muñoz, P. Palffy-Muhoray, B. Taheri, Advanced Materials 13 (2001) 1069.
[55] P.V. Shibaev, K. Tang, A.Z. Genack, V. Kopp, M.M. Green, Macromolecules 35 (2002) 3022.
[56] V.I. Kopp, Z.-Q. Zhang, A.Z. Genack, Physical Review Letters 86 (2001) 1753.
[57] S. Elston, R. Sambles, The Optics of Thermotropic Liquid Crystals, Taylor & Francis Inc., Pennsylvania, 1998.
[58] S. Teitler, B. Henvis, Journal of the Optical Society of America 60 (1970) 834.
[59] D.W. Berreman, Journal of the Optical Society of America 62 (1972) 502.

[60] H. Wohler, G. Haas, M. Fritsch, D.A. Mlynski, Journal of the Optical Society of America A 5 (1988) 1554.
[61] E. Yablonovitch, T.J. Gmitter, R.D. Meade, A.M. Rappe, K.D. Brommer, J.D. Joannopoulos, Physical Review Letters 67 (1991) 3380.
[62] Y.-C. Yang, C.-S. Kee, J.-E. Kim, H.Y. Park, J.-C. Lee, Y.-J. Jeon, Physical Review Letters E 60 (1999) 6852.
[63] V.I. Kopp, A.Z. Genack, US Patent No. 6 396 859, 2002.
[64] I.J. Hodgkinson, Q.H. Wu, K.E. Thorn, A. Lakhtakia, M.W. McCall, Optics Communications 184 (2000) 57.
[65] V.I. Kopp, R. Bose, A.Z. Genack, Optics Letters 28 (2003) 349.
[66] V.I. Kopp, A.Z. Genack, Physical Review Letters 89 (2002) 033901.